3

Solid Matter at Low Temperatures

The purpose of this chapter is to summarize the basic properties of solid materials at low temperatures [3.1–3.8] that are relevant for the design and construction of low-temperature apparatus and for performing experiments with such apparatus. These properties are, in particular, specific heat, thermal expansion, thermal conductivity and magnetic susceptibility. The latter property will also be discussed in later chapters in connection with magnetic cooling and thermometry.

Quite generally one can say that the properties of materials can be better understood when the temperature is reduced further (except for some exotic cases like solid ^{3}He), because as the temperature is lowered the properties of materials become more and more "ideal" or "simpler"; they approach their theoretical models more closely. At low temperatures the number of excitations decreases and the vibrations of the atoms can be described in the harmonic approximation, which means that the potential V^* as a function of distance $r - r_0$ from the equilibrium position r_0 of the atom can be written as

$$V^*(r - r_0) \propto (r - r_0)^2 \,. \tag{3.1}$$

In this approximation there is no thermal expansion because thermal expansion results from the anharmonic parts of the potential, for which we would have to introduce higher-order terms in the above equation. As a result, the thermal expansion coefficient becomes smaller and smaller, as we approach lower and lower temperatures (Sect. 3.2). A further advantage of low temperatures for the description of the properties of materials is the fact that various "parts" of a material can be treated independently. For example, in many cases one can consider the nuclear spin system (which is of great importance at ultralow temperatures) independently of the electrons and the lattice vibrations (Chap. 10). Of course, this is not true for all the "parts" of a material. For example, the temperature dependence of the electrical resistivity of a metal just results from the interaction of conduction electrons with the lattice. The fact that the specific heat and the thermal conductivity due to

F. Pobell, *Matter and Methods at Low Temperatures*

lattice vibrations and due to conduction electrons in the metal can be treated independently and can then just be added is a consequence of the large mass difference of the nuclei and electrons. To a very good approximation, their motions are independent, and the Schrödinger equation for the whole crystal can be separated into an electronic part and a lattice part. This is known as the Born–Oppenheimer approximation [3.1–3.5].

3.1 Specific Heat

The specific heat C is one of the most informative properties of a material. It is a measure of how much energy is necessary to increase the temperature of a material. In other words, it is a measure of the excited states of this material in the relevant temperature or energy range.

To calculate the specific heat of a material we therefore have to consider the various excitations that can be excited if we transfer thermal energy to it [3.1–3.8]. Hence, the specific heat carries a lot of information about the material.

3.1.1 Insulators

For nonmagnetic, crystalline insulators the most important, and in most cases only possible, excitations are vibrations of the atoms, the so-called phonons. At high temperatures all possible vibrational states of the atoms are excited. Considering each atom to behave as an independent, classical harmonic oscillator results in the Dulong–Petit law for the high-temperature specific heat of a material of N_0 atoms per mole, each of which has three degrees of freedom for its potential energy and for its kinetic energy. Because each degree of freedom contributes $k_\mathrm{B}/2$ to the specific heat (at constant volume of the material),

$$C_v = \frac{6}{2} N_0 k_\mathrm{B} = 3R = 24.94[\mathrm{J\,mol^{-1}\,K^{-1}}]\,. \tag{3.2}$$

However, when the thermal energy $k_\mathrm{B}T$ becomes of the order of the energy necessary for excitation of lattice vibrations one sees deviations from the Dulong–Petit law, because not all of the lattice vibrations will then be excited. The limit for the applicability of the Dulong–Petit law is given by

$$T \approx \hbar\omega_\mathrm{ph}/k_\mathrm{B}\,, \tag{3.3}$$

where ω_ph is the phonon frequency. The limiting temperature is of the order of a few 100 K.

In 1907 A. Einstein showed that a reasonable description of the specific heat of lattice vibrations below this temperature is obtained if the lattice vibrations are considered to be quantized. He performed a calculation of the phonon specific heat by describing the lattice vibrations as quantized phonon

"particles", but gave them all the same frequency ω_{E}. In this Einstein model the material is considered as being composed of independent oscillators with the energies

$$E_n = \hbar\omega_{\mathrm{E}}(n + 1/2)\,, \tag{3.4}$$

where $n = 0, 1, 2, \ldots$ is the excitation number of the modes or of the phonons. Planck then showed that the mean excitation number $\langle n\rangle$ of each oscillator or the mean number of phonons at temperature T is given by the Boson distribution function

$$\langle n\rangle = f_{\mathrm{ph}}(\omega) = \frac{1}{\exp(\hbar\omega/k_{\mathrm{B}}T) - 1}\,. \tag{3.5}$$

This model, of course, deviates from reality because the vibrational frequencies of the atoms in a crystal are not independent from each other. Due to the interatomic interactions they are not equal but are distributed over a spectrum, which can have a rather complicated structure as a function of energy (Fig. 3.1a). Again, at low temperatures the situation becomes simpler because the frequency dependence of the phonon density of states goes as ω^2 for low energies. As Debye showed, at low temperatures the phonon density of states g_{ph} can then be described by the following parabolic energy or frequency dependence (Fig. 3.1a):

$$g_{\mathrm{ph}}(\omega) = \begin{cases} (3V_{\mathrm{m}}/2\pi^2 v_{\mathrm{s}}^3)\omega^2 = 9N_0\omega^2/\omega_{\mathrm{D}}^3, & \omega < \omega_{\mathrm{D}}\,, \\ 0, & \omega < \omega_{\mathrm{D}}\,, \end{cases} \tag{3.6}$$

V_{m} being the molar volume, and v_{s} the average value of the longitudinal and transversal velocities of sound of a crystal: $v_{\mathrm{s}}^{-3} = (v_{\mathrm{long}}^{-3} + 2v_{\mathrm{trans}}^{-3})/3$.

Of course, this spectrum does not extend to infinity but is cut off at a maximum frequency that is given by the condition that g_{ph} contains all the $3N_0$ phonon frequencies,

$$\int_0^{\omega_{\mathrm{D}}} g_{\mathrm{ph}}(\omega)\mathrm{d}\omega = 3N_0. \tag{3.7}$$

This limiting frequency is called the Debye frequency ω_{D}. The corresponding temperature, the Debye temperature $\theta_{\mathrm{D}} = (\hbar/k_{\mathrm{B}})\omega_{\mathrm{D}}$ of the material, is a measure of the temperature below which phonons begin to "freeze out". Values for θ_{D} of several metals are given in Table 10.1. These parameters are material constants with large values for a lattice composed of light atoms which are strongly bound, as in diamond ($\theta_{\mathrm{D}} = 2{,}000\,\mathrm{K}$), and with small values for a lattice composed of heavy atoms bound by weak forces, as in lead ($\theta_{\mathrm{D}} = 95\,\mathrm{K}$).

If we apply the Debye model to calculate the internal energy of the lattice vibrations and take its temperature derivative to arrive at the specific heat,[1] we find [3.1–3.8]

[1] In the following I do not distinguish between C_{p} and C_{v}, the specific heats at constant pressure and constant volume, respectively; their difference $C_{\mathrm{p}} - C_{\mathrm{v}} = 9\alpha\kappa VT$ (α being the thermal expansion coefficient and κ the compressibility) is negligible for solids at low temperatures, approaching about 1% at $T \approx \theta_{\mathrm{D}}/2$.

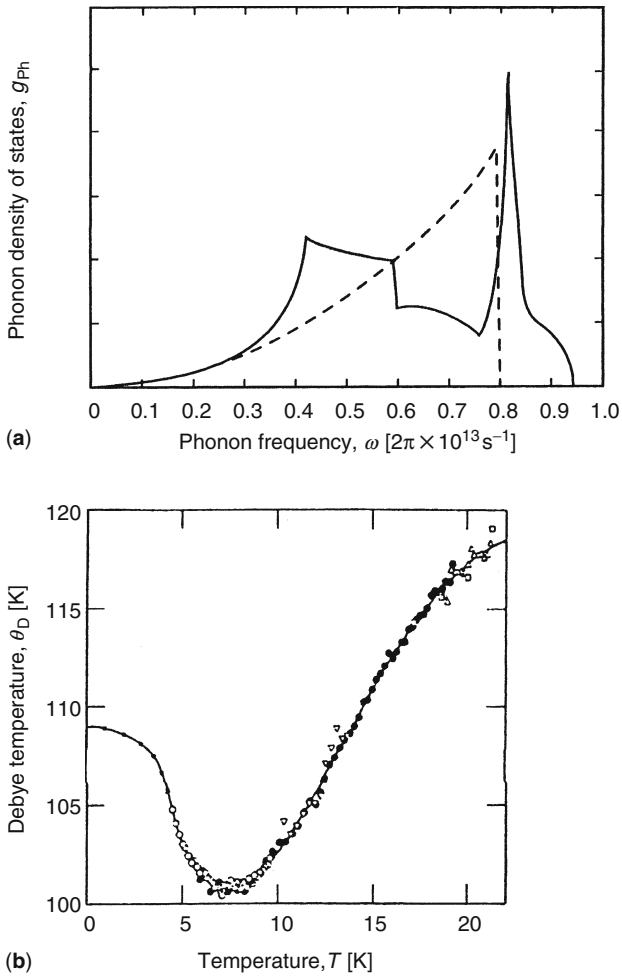

Fig. 3.1. (**a**) The phonon density of states $g_{\rm ph}$ measured at 300 K for aluminum. The dashed curve represents the Debye approximation (3.9) with a value $\theta_{\rm D} = 382\,{\rm K}$ deduced from the specific-heat data [3.9]. (**b**) Variation of the Debye temperature $\theta_{\rm D}$ of indium due to the influence of deviations from $g_{\rm ph} \propto \omega^2$ [3.10]

$$C_{\rm ph}(T) = 9N_0k_{\rm B}\left[\frac{T}{\theta_{\rm D}}\right]^3 \int_0^{x_{\rm D}} x^4\,{\rm e}^x({\rm e}^x-1)^{-2}{\rm d}x\,, \tag{3.8}$$

with $x = \hbar\omega/k_{\rm B}T$.

The integral yields

$$C_{\rm ph}(T) = \frac{12}{5}\pi^4 N_0 k_{\rm B}\left[\frac{T}{\theta_{\rm D}}\right]^3 = 1944\left[\frac{T}{\theta_{\rm D}}\right]^3 [{\rm J\,mol^{-1}\,K^{-1}}] \tag{3.9}$$

for temperatures $T < \theta_D/10$. A deviation of the phonon density of states from the ω^2 dependence can be taken into account by letting $\theta_D = f(T)$, see Fig. 3.1b. The cubic dependence of the phonon specific heat on temperature demonstrates its rather strong decrease with decreasing temperature. Therefore, insulators such as rare-gas crystals very often have a very small specific heat at low temperatures. Examples are illustrated in Fig. 3.2, which shows the good agreement between the Debye model and experimental data at low temperatures.

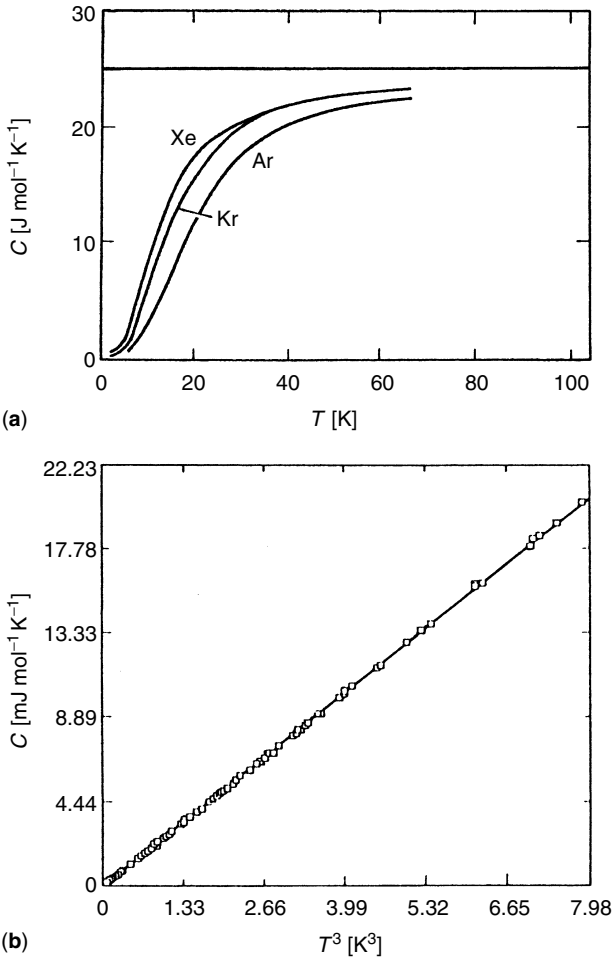

Fig. 3.2. (**a**) Specific heat of solid Ar, Kr and Xe. The horizontal line is the classical Dulong–Petit value [3.11]. (**b**) Specific heat solid of Ar as a function of T^3 at $T < 2\,\mathrm{K}$ [3.1, 3.12]

3.1.2 Metals

Besides the lattice vibrations, in a metal we also have (nearly free moving) conduction electrons, which can be thermally excited. Electrons have the spin 1/2, are fermions and obey the Pauli principle. Therefore, each energy state can be occupied by at most two electrons with antiparallel spin orientation. Putting all our electrons into energy states, we will fill these states up to a limiting energy, the Fermi energy, given by

$$E_{\mathrm{F}} = k_{\mathrm{B}}\, T_{\mathrm{F}} = \frac{\hbar^2}{2m}\left[\frac{3\pi^2 N_0}{V_{\mathrm{m}}}\right]^{2/3} = 3.0 \times 10^5 k_{\mathrm{B}}\, V_{\mathrm{m}}^{-2/3}\,[\mathrm{erg}]\,. \tag{3.10}$$

A typical value for this energy is 1 eV, corresponding to the rather high temperature of about 10^4 K. The Fermi–Dirac distribution function for the occupation of energy states of electrons at temperature T is (Fig. 3.3)

$$f_{\mathrm{e}}\,(E) = \frac{1}{\exp[(E-\mu)/k_{\mathrm{B}}T] + 1} \tag{3.11}$$

with the chemical potential $\mu = E_{\mathrm{F}}$ at $T = 0$. Because of the high value of the Fermi temperature $T_{\mathrm{F}} = E_{\mathrm{F}}/k_{\mathrm{B}}$, room temperature is already a "low temperature" for the electron gas, in the sense that here the electron gas is already pretty well in its ground state. And indeed, the properties of metals at low temperatures are determined exclusively by electrons in energy states very close to the Fermi energy.

To fill energy states we first have to determine them. That means, we have to calculate the density $g_{\mathrm{e}}(E)$ of states for conduction electrons. This is

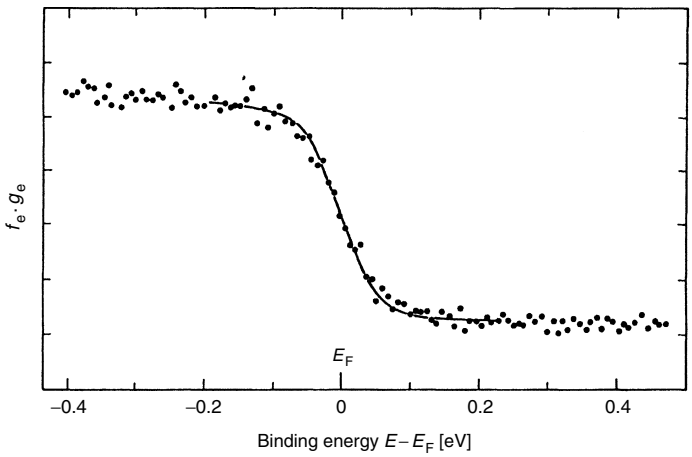

Fig. 3.3. Occupied electronic states of Ag at 300 K near the Fermi energy E_{F} obtained from photoelectron spectroscopy. The full line is the Fermi distribution function (3.11) [3.13]

rather simple within the "free-electron model", which describes many of the electronic properties of metals rather well [3.1–3.7]. The result is

$$g_{\mathrm{e}}(E) = \frac{3N_0}{2E_{\mathrm{F}}^{3/2}} E^{1/2} = \frac{V_{\mathrm{m}}}{2\pi^2} \left[\frac{2m}{\hbar^2}\right]^{3/2} E^{1/2} \,. \tag{3.12}$$

To find properties of the conduction electrons in a metal we have to multiply the two quantities $g_{\mathrm{e}}(E)$ and $f_{\mathrm{e}}(E)$.

At the temperature T one can thermally excite only electrons near the Fermi energy, within an energy range from about $E_{\mathrm{F}} - k_{\mathrm{B}}\,T$ to about $E_{\mathrm{F}} + k_{\mathrm{B}}\,T$; the thermal energy is not enough to excite electrons out of energy states further below the Fermi energy. At T the number of "thermally involved" electrons is then approximately given by $g_{\mathrm{e}}(E_{\mathrm{F}})\ k_{\mathrm{B}}\ T \propto T/T_{\mathrm{F}}$. If we raise the temperature from 0 to T, these electrons experience the energy change $\Delta E \simeq g_{\mathrm{e}}(E_{\mathrm{F}}) k_{\mathrm{B}}^2 T^2 \propto T^2/T_{\mathrm{F}}$ corresponding to an electronic specific heat of $C_{\mathrm{e}} \simeq 2g_{\mathrm{e}}(E_{\mathrm{F}}) k_{\mathrm{B}}^2 T$. If we perform the calculation more rigorously, we have to take into account the Fermi–Dirac distribution (3.11) at finite temperatures, which modifies our result for the electronic specific heat only slightly to

$$C_{\mathrm{e}}(T) = \frac{\pi^2}{2} N_0 k_{\mathrm{B}} \frac{T}{T_{\mathrm{F}}} = \gamma T \,, \tag{3.13}$$

where T_{F} is given by (3.10). The γ-values (Sommerfeld constants) for some metals are listed in Table 10.1. The result (3.13) is in good agreement with experimental data (Fig. 3.4) and was a great triumph for quantum mechanics, for the free-electron model, and for the Fermi theory of spin-1/2 particles.

Of course, for a real metal we have to give up the free-electron model. We have to consider the mutual interactions of the electrons, their interactions with the ions and the symmetry of the crystal. This can be taken

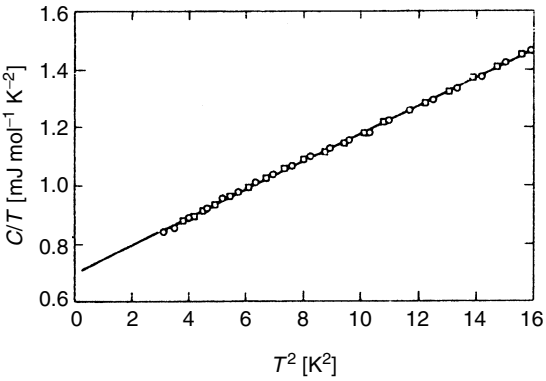

Fig. 3.4. Specific heat C of copper divided by the temperature T as a function of T^2 [3.4]

into account by going from the free-electron model to a so-called quasi-particle model [3.1–3.7]. In this model each electron has an effective mass m^* that deviates from the mass m of bare electrons because the electrons in a metal behave "heavier" or "lighter" than bare electrons owing to their interactions. We still obtain the same equations for the specific heat, in particular $C_e \propto T$; we just have to replace the mass of bare electrons by the effective mass of interacting electrons. For the specific heat, e.g., it means that we have to multiply (3.13) by m^*/m. The ratio of the effective mass m^* to the bare electronic mass m is between 1 and 2 for simple metals, it can be of order ten for transition metals with partly filled electron shells, and it can reach values of several 100 for "complicated" compounds, like the so-called "heavy-fermion" metals [3.5, 3.14, 3.15]. Values for the Sommerfeld constant γ for metallic elements can be found in condensed matter physics books [3.1–3.7].

With these results we arrive at the following equation for the total specific heat of a metal at "low" temperatures:

$$C = \gamma T + \beta T^3 \,. \tag{3.14}$$

"Low" means "small compared to the Debye temperature" if we consider the phonons and "small compared to the Fermi temperature" if we consider the electrons. If we introduce the appropriate material constants, we find that at room temperature the specific heat of a metal is dominated by the phonon specific heat and usually only at temperatures below 10 K is the electronic specific heat important; it dominates at temperatures below 1 K. The results for the electronic and lattice specific heats of copper are shown in Fig. 3.4, where C/T versus T^2 is plotted for low temperatures. The figure demonstrates how well the data are described by the theory discussed earlier. It also demonstrates that it is very often rather important to choose the right coordinates to get a sensitive indication of whether data follow an expected behavior.

3.1.3 Superconducting Metals

Many metals–elements, alloys and compounds–enter into a new state below a critical temperature T_c. In this so-called superconducting state [3.1, 3.2, 3.5, 3.6, 3.16–3.19] they can carry an electric current without dissipation, and they show several other new properties. As an example, I discuss here the specific heat of a metal in its superconducting state ($T < T_c$). Data for the specific heat of superconductors are presented in Fig. 3.5. Examining these data we arrive at the following conclusions. The specific heat C_{ph} of the lattice vibrations is not influenced by the transition to the superconducting state. It still follows a T^3 law with the same coefficient as one finds in the normal-conducting state (3.9)

$$C_{ph,\,s} = C_{ph,\,n} = \beta T^3 \,. \tag{3.15}$$

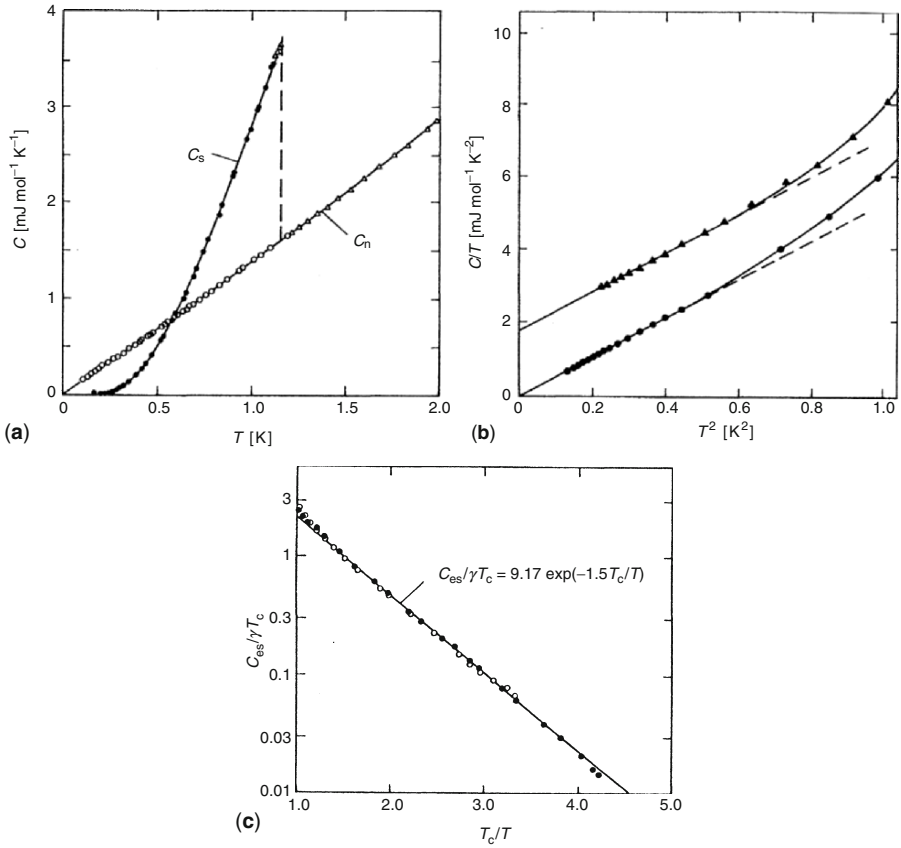

Fig. 3.5. (**a**) Specific heat of Al in the superconducting (C_s) and normal-conducting (C_n) states [3.20]. (**b**) Specific heat C of Hg divided by temperature T as a function of T^2 in the normal (▲) and superconducting (●) states. The straight lines correspond to (3.9,3.13) with $\theta_D = 72\,K$ and $\gamma = 1.82\,mJ\,mol^{-1}\,K^{-2}$ [3.21]. For the measurements in the normal conducting states, a magnetic field $B > B_c$ had to be applied to suppress the superconducting state. (**c**) Electronic specific heat C_{es} of superconducting V (●) and Sn (○) divided by γT_c as a function of T_c/T. The full line represents (3.17) [3.22]

The new behavior evident from Fig. 3.5 is entirely due to the altered specific heat of the electrons. First of all, there is a jump of the electronic specific heat at the critical temperature, but no latent heat (the transition is a second-order phase change when the external magnetic field is zero). The jump in C occurs because the metal now has – one might say – a new "degree of freedom" corresponding to the possibility of entering the superconducting state. In the discussion of the Dulong–Petit law for the specific heat at high temperatures we have already seen that each degree of freedom enhances the

specific heat. For simple superconductors such as aluminum and tin, which follow the Bardeen, Cooper, Schrieffer (BCS) theory of superconductivity [3.1, 3.2, 3.5, 3.6, 3.16–3.19, 3.23], the jump of the specific heat is given by

$$\Delta C = 1.43\gamma T_{\mathrm{c}}\,, \tag{3.16}$$

where γT_{c} is the normal-state electronic specific heat (3.13) at T_{c}.

Below the transition temperature the electronic specific heat in the superconducting state vanishes much more rapidly than the electronic specific heat in the normal–conducting state of the metal. Its temperature dependence for "simple", so-called weak-coupling BCS superconductors [3.23] is given by

$$C_{\mathrm{e,\,s}} = 1.34\gamma T_{\mathrm{c}}(\Delta E/k_{\mathrm{B}}T_{\mathrm{c}})\exp[-\Delta E/k_{\mathrm{B}}T_{\mathrm{c}}] \tag{3.17}$$

An exponential temperature dependence of the specific heat is indicative of an energy gap ΔE in the density of states, as it occurs for the electrons in a superconductor (and in a semiconductor). This reflects the number of electrons thermally excited across the energy gap.

3.1.4 Non-crystalline Solids

In noncrystalline or disordered solids [3.5, 3.24–3.28] like vitreous silica or metallic glasses the atoms are not arranged in a periodic order; these solids can be visualized as supercooled liquids. As an example, Fig. 3.6 depicts a possible arrangement of silicon and oxygen atoms in vitreous silica compared to crystalline quartz. In such a disordered structure where long-range order is lost many atoms have more than one possible position and these positions can be distinguished by rather small energy differences. Even at low temperatures the atoms can "tunnel" from one position to another. Again, we have a new "degree of freedom" for the material: the possibility of performing

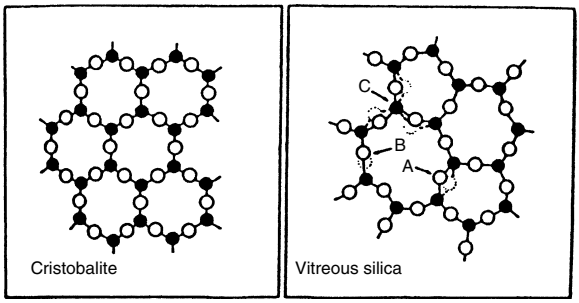

Fig. 3.6. Schematic two-dimensional representation of the structure of cristobalite, a crystalline modification of SiO_2, and of vitreous silica, the amorphous modification of SiO_2. Filled circles represent silicon atoms and open circles oxygen atoms. Three possible types of defects are indicated by arrows [3.5, 3.26]

structural rearrangements. As a result, we observe an additional contribution to the specific heat caused by the tunneling transitions or structural relaxations in a disordered or glassy material. At low temperatures this additional contribution dominates and is given by

$$C_{\mathrm{a}} = aT^n \tag{3.18}$$

with an exponent n which is close to 1 [3.5, 3.24–3.30]. (In addition, one often observes an enhancement of the T^3 specific heat contribution.) This is illustrated for vitreous silica in Fig. 3.7. Disordered insulators, therefore, show an almost linear contribution (from the tunneling transitions between various positions of the atoms) and a cubic contribution (from the vibrations of the atoms) to the specific heat. The same is observed for a metallic glass, but here we have two contributions to the linear part of the specific heat, one from the tunneling transitions and the other one from the conduction electrons. It is very remarkable that the contributions to the specific heat from the non-crystallinity are of very similar size even for quite dissimilar

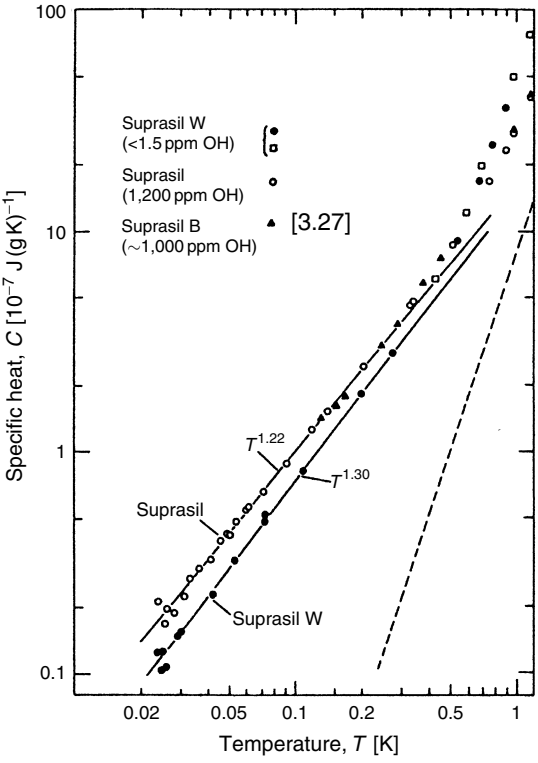

Fig. 3.7. Specific heats of three types of vitreous SiO_2 containing different concentrations of OH^- (as well as metal ions, chlorine and fluorine). The dashed line is the phonon specific heat of crystalline SiO_2 [3.29]

materials [3.5, 3.24–3.30], indicating that the additional excitations in a disordered material are associated with the disorder and do not depend on the type of material very much. Because the specific heat contributed by disorder decreases linearly with decreasing temperature instead of as T^3 as for lattice vibrations, the specific heat of a dielectric in its glassy state is much higher than in its crystalline state at low temperatures (Fig. 3.7). Often, below about 1 K, glasses have a specific heat which is even larger than that of a metal. In fact, at 10 mK the heat capacity of a dielectric glass can be a factor of 10^3 larger than the heat capacity of the corresponding crystal, which can be of great importance for the design of a low-temperature apparatus containing noncrystalline components. The heat capacities of some disordered dielectrics often used in a cryogenic apparatus are given in Sect. 3.1.7.

3.1.5 Magnetic Specific Heat

When a magnetic field is applied to a material whose atoms have magnetic moments, there are $(2I + 1)$ ways the magnetic moments can orient themselves with respect to the magnetic field, I being the spin associated with the magnetic moment. Again, a new "degree of freedom" results in an additional contribution to the specific heat. Let us consider the simplest case, a spin-1/2 system so that there are two possible spin orientations, and they should have equal degeneracy. At very low temperatures most of the magnetic moments will be in the lower energy state. If the temperature increases, transitions from the lower to the upper level will occur, giving the following contribution to the specific heat [3.1–3.6]:

$$C_{\mathrm{m}} = N_0 k_{\mathrm{B}} \left[\frac{\Delta E}{k_{\mathrm{B}} T}\right]^2 \frac{\mathrm{e}^{\Delta E/k_{\mathrm{B}}T}}{(1+\mathrm{e}^{\Delta E/k_{\mathrm{B}}T})^2}\,. \tag{3.19}$$

This contribution, shown in Fig. 3.8, is called a Schottky anomaly. Very often the energy splitting ΔE is small compared to the thermal energy $k_{\mathrm{B}}T$. In this "high-temperature" approximation the magnetic contribution to the specific heat is given by

$$C_{\mathrm{m}} \;\Rightarrow\; N_0 k_{\mathrm{B}} \left[\frac{\Delta E}{2k_{\mathrm{B}}T}\right]^2 \quad \text{for } \Delta E \ll k_{\mathrm{B}}T\,. \tag{3.20}$$

For a metal with such a T^{-2} contribution we have for the specific heat at $T < 1$ K where the lattice specific heat is negligible

$$C = \gamma T + \delta T^{-2}\,. \tag{3.21}$$

The magnetic specific heats of some commercial alloys containing paramagnetic atoms and being often used as thin wires for low-temperature equipment are exhibited in Fig. 3.9. Again, at $T < 1$ K, the specific heat can be strongly enhanced compared to the simple electronic and lattice specific heats.

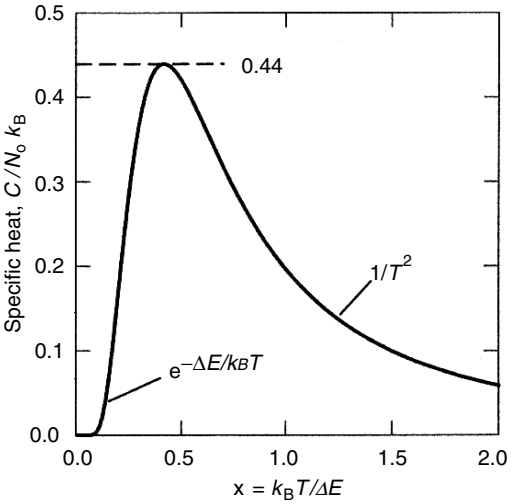

Fig. 3.8. Specific heat C (divided by $N_0 k_\mathrm{B}$) of a two-level system with energy separation ΔE

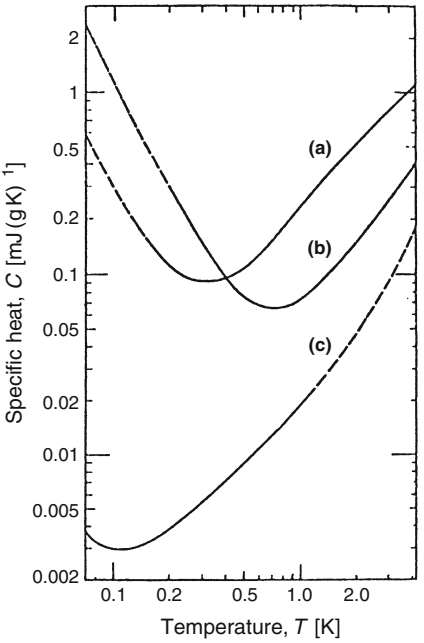

Fig. 3.9. Specific heats of (**a**) Constantan (57% Cu, 43% Ni), (**b**) Manganin (87% Cu, 13% Mn) and (**c**) a 9% W, 91% Pt alloy [3.31]. Similar values, as plotted in (**a**) and (**b**), have been reported for stainless steel in [3.32]; see also Sect. 3.1.7

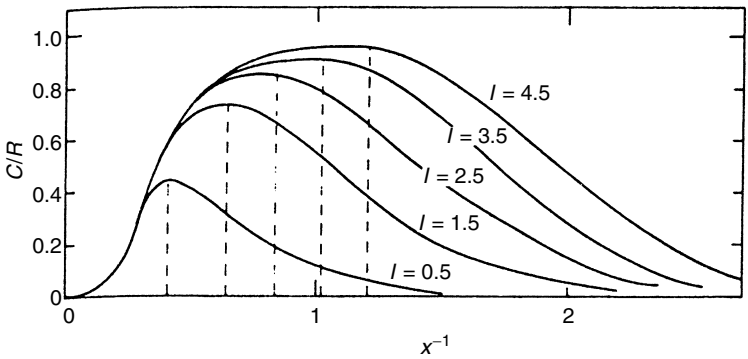

Fig. 3.10. Molar heat capacities C divided by the gas constant R as a function of $1/x_e = k_B T/g_e \mu_B B$ or $1/x_n = k_B T/g_n \mu_n B$ for different values of spin I (see also Table 3.1)

The data in Fig. 3.9 demonstrate that one has to be very cautious in employing wires of manganin (87% Cu, 13% Mn) or Constantan (57% Cu, 43% Ni) at $T < 1\,\mathrm{K}$ and, in fact, it would be better to resort to other commercial materials, like 92% Pt, 8% W.

Of course, in general the spin may be larger than 1/2 and we then have more than two levels. The calculation of the Schottky specific heat using (9.15b) for $I = 0.5$, 1.5, 2.5, 3.5 and 4.5 in Fig. 3.10 reveals that this results only in quantitative changes. But for low-temperature physics it is rather important to remember that the *temperature* at which the maximum of the magnetic contribution to the specific heat occurs is determined by the energy splitting ΔE of the levels. In other words, for nuclear magnetic moments, which are about a factor of 1,000 smaller than electronic magnetic moments, this maximum occurs at much lower temperatures than for the electronic magnetic moments. For example, an electronic magnetic moment of $1\,\mu_B$ in a field of 1 T leads to a maximum in C_m at about 1 K, whereas a nuclear magnetic moment in this field will have a maximum in C_m at only about 1 mK (Chaps. 9 and 10). But the *maximum value* of the specific heat is *independent* of the energy splitting, it is only a function of the number of degrees of freedom $(2I + 1)$; these values are listed in Table 3.1. This means that an electronic paramagnet with a spin 1/2 in an arbitrary external magnetic field will have $C_{m,max} = 0.439\,R$ (occurring in the Kelvin range or possibly at even higher temperatures, depending on the magnitude of its moment and the magnetic field this moment is exposed to). On the other hand, a nuclear magnetic moment, again with a spin 1/2, will have the *same maximum value* of the specific heat, but occurring at much lower temperature, in the microkelvin or millikelvin temperature range due to its smaller moment. This fact is of considerable importance for nuclear magnetic refrigeration (Chap. 10).

Table 3.1. Position $x_{\max}$ of $x_{\mathrm{e}} = g_{\mathrm{e}}\mu_{\mathrm{B}}B/k_{\mathrm{B}}T$ or $x_{\mathrm{n}} = g_{\mathrm{n}}\mu_{\mathrm{n}}B/k_{\mathrm{B}}T$ and value $(C_{\max}/R)$ of the maximum of the magnetic specific heat divided by the gas constant, as a function of spin (or angular momentum) I (see also Fig. 3.10)

I:	1/2	3/2	5/2	7/2	9/2
$x_{\max}$	2.399	1.566	1.193	0.976	0.831
$C_{\max}/R$	0.439	0.743	0.849	0.899	0.927

A good example for a specific heat composed of a lattice T^3 term and a nuclear–magnetic T^{-2} term is the specific heat of solid ^{3}He depicted in Fig. 8.3.

The above considerations on specific-heat contributions resulting from interactions between a magnetic moment and a magnetic field can be applied analogously to the specific heat resulting from interactions of an electric quadrupole moment with an electric field gradient (see also Sects. 3.1.6 and 10.6).

3.1.6 The Low-Temperature Specific Heat of Copper and Platinum

Copper is a material that is particularly important and often used in a low temperature apparatus. There are several reports in the literature of an enhanced specific heat of Cu at low temperatures [3.33–3.42]. For $0.03\,\mathrm{K} \leq T \leq 2\,\mathrm{K}$ these increases have been traced to hydrogen and/or oxygen impurities, to magnetic impurities, mainly Fe and Mn, and to lattice defects [3.35–3.42]. On the other hand, the increased specific heat of Cu observed in the low millikelvin temperature range may also arise from a nuclear quadrupole Schottky-type contribution, see (10.35), due to Cu nuclei (which have a nuclear quadrupole moment) being located in noncubic neighbourhoods, which occur near lattice defects or in copper oxide [3.41, 3.42] (Fig. 3.11). These anomalies should be considered in the wide-spread low-temperature applications of Cu in calorimetry, thermometry (Chap. 12) and nuclear–magnetic cooling (Chap. 10), and in other applications of this very useful metal. A proper heat treatment of Cu may remove some of these anomalous increases of the specific heat.

Platinum is the "workhorse" of thermometry at low mK and at μK temperatures (Sect. 12.10.3). Hence, it is important to know that its low-temperature properties are strongly influenced by small concentrations of magnetic impurities. As, for example, reported in [3.43], Fe impurities in the ppm range increase the specific heat of Pt at 1 mK and in a field of 11 mT by about an order of magnitude. This effect is caused by the giant moments of 8 μ_B of the Fe impurities in Pt.

3.1.7 Specific Heat of Some Selected Materials

Comprehensive compilations of data and references to specific heat values, including values for technically important materials, can be found in

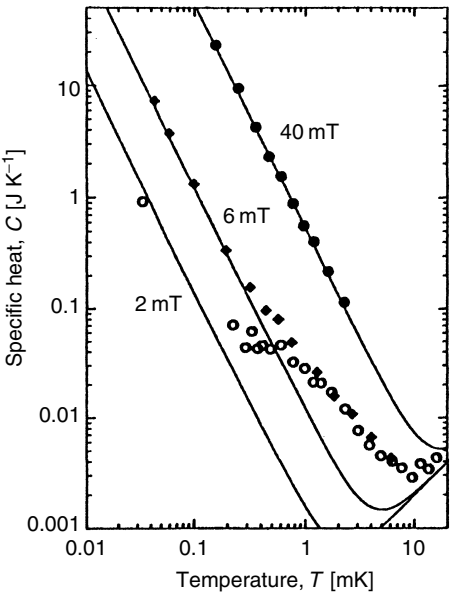

Fig. 3.11. Heat capacity of 275 mol of Cu, of which 104 mol are in the given magnetic fields, as a function of temperature. The full lines are the expected values for the nuclear magnetic heat capacities of 104 mol Cu in the given fields plus – at higher temperatures – the electronic contributions of 275 mol Cu. The deviation of the measured data from the lines is attributed to a heat capacity resulting from a splitting of the $I = 3/2$ nuclear levels of Cu due to a nuclear electric quadrupole interaction, see (10.35), of 11 mmol of Cu which are located in an electric field gradient of about $10^{18}\,\mathrm{V\,cm^{-2}}$. For these Cu nuclei the cubic symmetry must have been destroyed in order to create an electric field gradient [3.42]

[3.7, 3.44–3.48]. Some of these data are depicted in Fig. 3.12. References [3.7, 3.44] contain a compilation of data at 25, 50, 75, 100, 150, 200, 250, and 293 K for several metallic elements as well as for some alloys, non-metals, and polymers often used in the construction of cryogenic apparatus. In the following, I will supplement these compilations with some additional data for often used materials, in particular at lower temperatures. All data are given in units of $\mu\mathrm{J\,g^{-1}\,K^{-1}}$.

Metals

Be–Cu: $\mathrm{C} = 3.58\ 10^{-3}\ \mathrm{T}^{-1.64}$ at 0.5–5 mK (!) [3.49]
Constantan: $\mathrm{C} = 205\ \mathrm{T} + 2.8\ \mathrm{T}^{-2}$ at 0.15 – 0.3 K as well as data to 4 K in [3.31]
Cu: see [3.33, 3.34, 3.50]
Manganin: $\mathrm{C} = 59.5\ \mathrm{T} + 2.94\ \mathrm{T}^3 + 11.5\ \mathrm{T}^{-2}$ at 0.2–2.5 K as well as data to 4 K in [3.31]
$\mathrm{Pt_{91}} - \mathrm{W_9}$ heater wire: $\mathrm{C} = 17.6\ \mathrm{T} + 1.4\ \mathrm{T}^3 + 0.12\ \mathrm{T}^{-2}$ at 0.07–1.2 K [3.31]

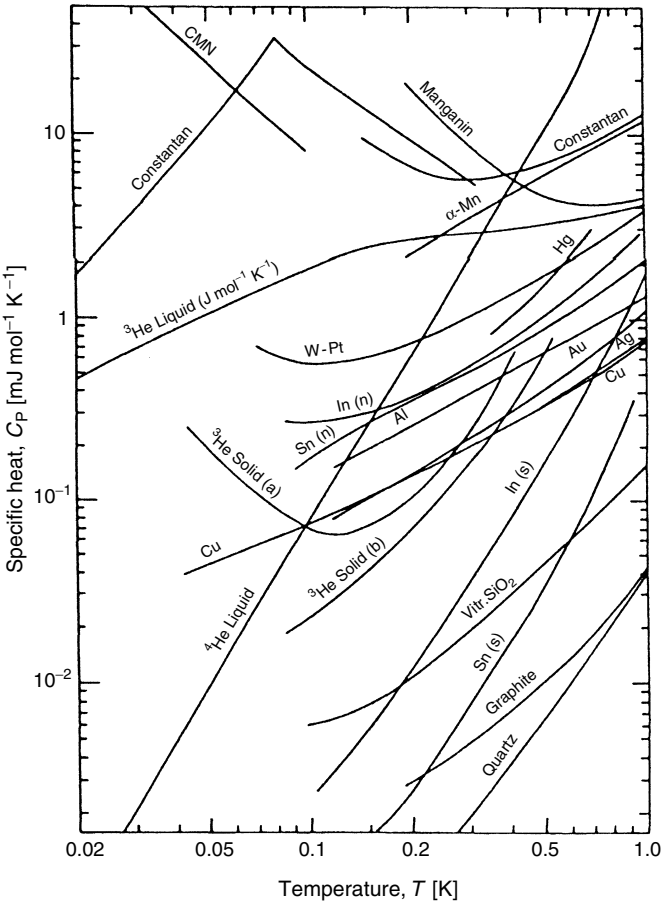

Fig. 3.12. Specific heats of several materials below 1 K [3.45]. (This publication provides references to the original literature)

Stainless steel 304: $C = 465\ T + 0.56\ T^{-2}$ at 0.07–0.6 K [3.32]
$C = 460\ T + 0.38\ T^3$ at 1–10 K [3.51]

Dielectrics

Apiezon N grease: $C = 1.32\ T + 25.8\ T^3 + 0.0044\ T^{-2}$ at 0.1–2.5 K [3.52]; data at 16–319 K can be found in [3.53]
G 10 Composite: $C = 4.74 \times 10^3\ T^{0.912}$ at 100–350 K and values to 1.8 K from [3.54]
GE 7031 varnish: $C = 6.5\ T + 19\ T^3$ below 1 K [3.28]
Stycast 1266 epoxy: $C = 2.91\ T + 15.7\ T^3 + 8.98\ T^5$ at 0.1–1 K [3.72]
Stycast 2850FT epoxy: data at 1 to 95 K with $C = 12$ at 1 K [3.55]
Polypropylene: $C = 6.15\ T^{1.33} + 20\ T^3$ at 0.06–1 K [3.56]

PMMA: $C = 3.0\ T + 77\ T^3$ at 0.07–0.2 K [3.57]
$C = 4.6\ T\ + 29\ T^3$ below 1 K [3.28]
Polystyrene (PS): $C = 4.6\ T + 93\ T^3$ at 0.07–0.2 K [3.57].

3.1.8 Calorimetry or How to Measure Heat Capacities

To measure a heat capacity C, we have to refrigerate the material of mass m to the starting temperature T_i, isolate it thermally from its environment (for example, by opening a heat switch; see Sect. 4.2), and supply some amount of heat P to reach the final temperature T_f. The result is $C/m = P/(T_f - T_i)$ at the intermediate temperature $T = (T_f + T_i)/2$. An essential problem for the accuracy of heat-capacity measurements is the fact that it is not the temperature but the much smaller and therefore often much less accurately known temperature difference which matters. There are several other problems that have to be carefully considered for accurate heat-capacity measurements which I will mention in the following.

A calorimeter consists of a platform to which sample, thermometer, and heater are connected, usually by glue or epoxy (Fig. 3.15). For the adiabatic heat-pulse method, a heat switch is necessary to connect and disconnect the calorimeter to a bath. The heat capacities of the addenda should be small compared to that of the sample or they have to be known with sufficient accuracy from a measurement without sample so that they can be subtracted from the total value to obtain the heat capacity of the sample. The leads to the thermometer and heater have to be of low thermal conductivity (the best are, of course, thin superconducting wires at the low-temperature end) and have to be carefully heat-sunk at a temperature close to the temperature of the calorimeter to avoid heat flow into it. Thermometer, heater and sample should, of course, be well thermally coupled to the platform to avoid unknown temperature differences (see the thermal boundary problems discussed in Sect. 4.3). The power needed to read the thermometer should be small to avoid overheating it. Calibration of the thermometer and measurement of the heat capacity should be performed with the same power applied to the thermometer to have in both cases the same unavoidable, hopefully small temperature difference between thermometer and platform. Parasitic heat losses or heat inflow by radiation can be reduced by a thermal shield around the calorimeter with a temperature regulated closely to the temperature of the calorimeter [3.33, 3.58, 3.59]. Heat produced by opening and/or closing a mechanical (Sect. 4.2.1) or a superconducting (Sect. 4.2.2) heat switch has to be small. When exchange gas is used for the cooldown of the calorimeter, it has to be pumped away before performing the measurement, which is usually quite time-consuming. Still, one has to take into account the possibility of adsorption and desorption of residual gas when the temperature is changed. This produces heat of adsorption/desorption, which is on an order of magnitude of the large heat of vaporization. Eventually, time constants for thermal equilibrium within the sample, within the addenda and between sample and addenda have to be considered.

As a result of these problems, heat-capacity data rarely have an accuracy better than 1%, more usual are accuracies of 3–5% (but see below). If a high accuracy is needed or if the parameters of the setup are not well known, the quality of a calorimeter can be checked by measuring the heat capacity of a well-known reference sample like high purity Cu [3.33, 3.34, 3.50].

Substantial advances in calorimetry have been achieved due to the development of high-performance electronics, new thermometers, micro-fabrication techniques, and computer automation. However, one has to keep in mind that the properties of the thermometer (as well as the accuracy of the used temperature scale) is the essential parameter for the accuracy of heat-capacity data. High-resolution heat-capacity data can only be obtained when the relevant precautions are taken and when a calibrated, sensitive, and stable thermometer is used.

There are a myriad of reports on the design, construction, and operation of calorimeters; most of them can be found in the journal Review of Scientific Instruments. Therefore, the selection of calorimeters to be discussed in this section surely is a subjective choice. In the following, I will discuss a few of the more recent elegant or versatile designs for the usual adiabatic heat-pulse method. This will be followed by a discussion of calorimeters for situations where this straightforward adiabatic approach of applying heat and measuring the temperature increase of the thermally isolated calorimeter is inadequate and more sophisticated methods have to be used; for example, for very small samples or in hostile environments, like high magnetic fields or pressures, or for the investigation of sharp features at a phase transition.

Surely, the champion of adiabatic heat-pulse calorimetry with respect to temperature resolution and temperature stability is the measurement of the heat capacity C of liquid ^{4}He near its superfluid transition [3.59]. In these experiments, C has been measured with sub-nanokelvin resolution at temperatures to within about a nanokelvin of the transition temperature $T_\lambda = 2.177\,\mathrm{K}$ (see Fig. 2.10b). Such an extreme temperature resolution is only meaningful for the investigation of a phase transition of liquid helium because only in this substance purity and perfection are high enough so that the phase transition shows the required sharpness. In all other materials, phase transitions are smeared by impurities and by imperfections of the structure. In addition, this measurement had to be performed in flight on earth orbit to reduce the rounding of the transition caused by gravitationally induced pressure gradients and therefore spreading the transition temperature over the liquid sample of finite height. The high-resolution magnetic susceptibility thermometers developed for these experiments are described in Sect. 12.9. In the used experimental setup, four thermal control stages in series with the calorimeter were actively temperature regulated; the last one to a stability of less than $0.1\,\mathrm{nK\,h^{-1}}$. Besides this thermal regulation, the experiment required very careful magnetic shielding, in particular of the electric leads as well as extremely low electric noise levels. Even though this surely is not a typical laboratory heat-capacity experiment, a lot can be learned from the

chosen design, the precautions, and detailed considerations of possible error sources [3.59], which could be quite useful for simpler experiments on earth.

Another quite remarkable achievement was the adiabatic measurement of the nuclear magnetic heat capacity of $AuIn_2$ to temperatures of 25 μK in an investigation of its *nuclear* ferromagnetic transition at 35 μK [3.60]. In this temperature range, nuclear magnetic resonance on ^{195}Pt (Sect. 12.10.3) is the only available method of thermometry, making the calorimeter quite demanding; it is shown in Fig. 3.13. This example demonstrates that the addenda can

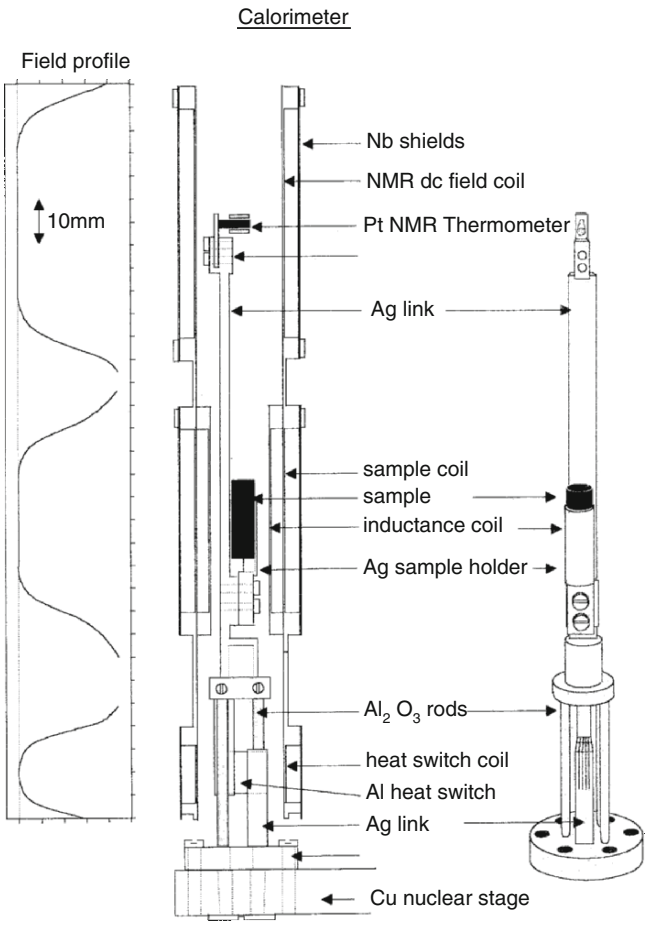

Fig. 3.13. Schematic of a calorimeter used to measure the nuclear heat capacity (Fig. 3.14) as well as the nuclear AC susceptibility of a $AuIn_2$ sample at microkelvin temperatures. The calorimeter is connected via a superconducting Al heat switch (Sect. 4.2.2) to a Cu nuclear refrigeration stage (Sect. 10.8). It contains a Pt NMR thermometer (Sect. 12.10.3). The calorimeter is surrounded by coils for magnetic DC fields for the NMR thermometer, the sample, and the heat switch, as well as by superconducting Nb shields (Sect. 13.5.2), [3.60]

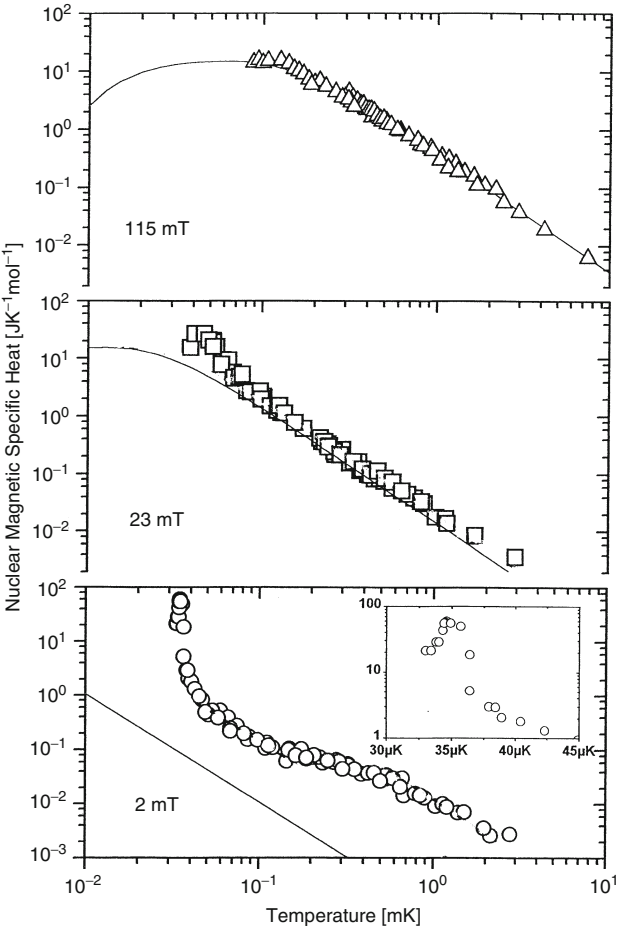

Fig. 3.14. Nuclear magnetic specific heat of In nuclei in $AuIn_2$ per mole of the compound (per 2 moles In) in the three indicated magnetic fields. The full lines are the Schottky curves (see 3.19 and 3.20, as well as Fig. 3.10) for non-interacting In nuclei (I=5/2) in the given external fields. The lower two figures demonstrate the enhancement of the heat capacity by the interaction of the In nuclei which gives rise to a nuclear ferromagnetic ordering of them at 35 μK, shown more clearly in the inset. The heat capacity at the ordering transition is enhanced by the interactions of the small In nuclei by three orders of magnitude at 2 mT; it has about the value as Co has at its Curie temperature of 1390 K (!) [3.60]

be large as long as its heat capacity is small compared to that of the sample, in this case the huge nuclear heat capacity of $AuIn_2$ at microkelvin temperatures. The obtained data shown in Fig. 3.14 also demonstrate how large a magnetic heat capacity can become even at very low temperatures independently of

whether it is caused by the electronic or by the much smaller nuclear magnetic moments; it is determined by the spin degeneracy. And eventually, talking about heat-capacity measurements under extreme conditions, heat-pulse calorimetry performed in pulsed magnetic fields up to $60\,T$ should be mentioned [3.61]. Here, it is essential to avoid any material with magnetic moments or containing magnetic impurities in the addenda (to keep its heat capacity small) and to use pure, but electrically badly or non-conducting materials (to reduce eddy current heating) as far as possible, like single crystalline Si or high-purity plastics as platform. Of course, the choice of the appropriate thermometer – mostly a resistor – with very low field dependence (see Sect. 12.5) is of particular importance.

All these mentioned calorimeters used the conventional adiabatic heat-pulse technique. A semi-adiabatic heat-pulse technique without heat switch but with the sample and platform weakly connected to the bath at 30 mK via the appropriately chosen conductance of mounting threads and electrical leads is described in [3.62]. In this calorimeter, parasitic heat leaks or thermal losses have been compensated through an adjustable background heating to assure a constant temperature of the platform. The heat capacity of milligram samples was measured at 0.03–6 K in magnetic fields up to $12\,T$.

In particular for measurements of the heat capacity of small samples, other methods like the thermal relaxation time technique or the AC calorimetric technique with a calorimeter weakly coupled to a thermal bath at constant temperature should be used (Fig. 3.15). In the *thermal relaxation method* [3.64–3.67] heat is applied for a fixed time to sample and addenda, and then the exponential thermal relaxation back to the bath temperature is recorded. The heat capacity C is determined from the relaxation time $\tau_1 = C/k_1$ with $C = C_{\text{sample}} + C_{\text{addenda}}$ and k_1 the thermal conductance of the weak link to the bath. Both the thermal conductance k_1 and the addenda heat capacity have to be determined independently. The relaxation time τ_1 has to be larger than all internal relaxation times of the system, otherwise the relaxation is not a single exponential curve. This means in particular that the conductance between the sample and the platform has to be much larger than k_1. The sensitivity is determined by the quality of the thermometer and by the (as small as possible) heat capacity of the addenda. This method can have rather high absolute accuracy, however, its relative accuracy is limited.

This is just the opposite for the *AC method*, which can detect very small changes in the heat capacity [3.63, 3.65, 3.68]. Here, heat P is applied sinusoidally and the resulting temperature oscillation at frequency ω is determined. It is $\delta T = (P/\omega C)(1 + \omega^{-2}\tau_1^{-2} + \omega^2\tau_2^2)^{-1/2}$ with τ_2 the relaxation time within the calorimeter assembly and τ_1 the relaxation time of the calorimeter to the bath. In the usual limit $\omega\tau_1 \gg 1 \gg \omega\tau_2$, the heat capacity $C = P/\omega\delta T$. To check whether this limit has been achieved, the temperature response has to be measured at various frequencies – typically between a few and 200 Hz – to determine below which frequency heat escapes through the thermal link to the bath within the measuring period and above which

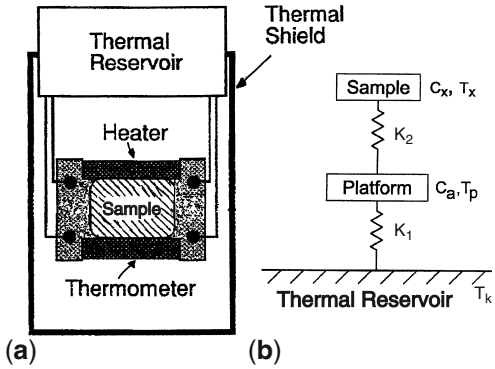

Fig. 3.15. (**a**) Schematic of a setup for heat-capacity measurements by the thermal relaxation or the AC techniques. A platform (for example, a thin sapphire or silicon disc or a membrane) carries sample, heater and thermometer. It is weakly coupled to a thermal reservoir at constant temperature and surrounded by a thermal shield. For high accuracy measurements, the temperature of the shield is regulated close to the temperature of the platform. Leads to heater and thermometer are thermally grounded at the thermal reservoir and then at the platform; they can also serve as weak thermal link between platform and reservoir as well as mechanical support. The set–up can be used for the more conventional heat-pulse technique by adding a heat switch between reservoir and platform. (**b**) Heat flow diagram for the shown setup. The sample of heat capacity C_x and at temperature T_x is connected via a thermal link of conductance k_2 to the platform with heat capacity C_a and at temperature T_p. The thermal link between platform and thermal reservoir has the conductance k_1. C_a contains the contributions from platform, thermometer, heater, and their mounting (glue, grease, varnish,...); it should be substantially smaller than C_x and has to be measured independently. Similarly, the conductance k_2 should be much larger than k_1

frequency the calorimeter can not follow anymore the heat modulation; i.e., to see in which frequency range a steady state can be reached where $\delta T\omega$ is independent of frequency. A simplified version of the relaxation method is the so-called "dual slope method" [3.69]. Here, the sample plus addenda are continuously heated and cooled, and the specific heat at temperature T is derived from the slopes of these two cycles at T.

In the calorimeters for these techniques, usually the sample holder is a small chip (for example, thin silicon or sapphire) or membrane, to which the heater, thermometer, and sample – with the latter having hopefully a substantially higher heat capacity than all the other parts – are mounted. This device is hanging in vacuum by means of thin supporting wires that provide a weak and controllable thermal link to the bath and can serve also as electrical leads for thermometer and heater (Fig. 3.15). Various micro-thermometers and nonmagnetic, temperature-independent resistive heaters (for example, NiCr or TiCr alloys) have been developed for this purpose (see various references in this section).

In [3.66], the relaxation method has been used with an amorphous silicon-nitride membrane, supported by a silicon frame, onto which thin-film heaters and thermometers (Pt for $T > 50\,\mathrm{K}$, amorphous NbSi or boron doped Si for lower temperatures) are patterned. The heat capacity of this addendum is $<1\,\mathrm{nJ\,K^{-1}}$ at 2 K and $6\,\mu\mathrm{J\,K^{-1}}$ at 300 K only. This calorimeter has been used to investigate microgram samples or thin films in steady fields up to 8 T; according to the authors, it should be usable also in pulsed fields up to 60 T. This is the result of the rather weak dependence of the properties of the calorimeter parts on magnetic field (for example, their conductances and the weak magnetoresistance of the used thermometers), and of the fact that in a very good approximation the relaxation time does not rely on the calibration of the thermometer. Reference [3.66] gives a detailed description of the fabrication and properties of this calorimeter and all its components. A relaxation calorimeter for use in a top-loading ^{3}He-^{4}He dilution refrigerator in high magnetic fields has been described in [3.67]. It has been used for milligram samples from 34 mK to 3 K and in magnetic fields up to 18 T. In order to keep thermal time constants in the magnetic field reasonably short, most of the addenda like the thermal reservoir are made from Ag, which has one of the smallest nuclear heat capacities of suitable materials (see Fig. 10.4 and Table 10.1).

In an elegant version of a calorimeter for microgram samples of [3.65], a modified commercial thin-film ceramic silicon oxynitride chip of $1 \times 0.75 \times 0.1\,\mathrm{mm^3}$ ("Cernox", see Sect. 12.5.3) was used simultaneously as sample holder and temperature sensor, with a $Ni_{80}Cr_{20}$ heater sputtered onto it. This calorimeter of only 0.25 mg weight was used for the relaxation as well as for the AC methods at 1.5–50 K and in magnetic fields up to $11\,T$ (Cernox is rather insensitive to magnetic fields, see Sect. 12.5.3). According to the authors, the sensitivity of this calorimeter over the whole temperature range is a factor of 100 higher than that of a comparable commercial calorimeter (see below), using a silicon-on-sapphire design. The most sensitive microcalorimeters have been built by the group of Chaussy [3.68]. In their latest version, these AC calorimeters for the Kelvin temperature range consist of a 2 to 10-μm-thick monocrystalline silicon membrane substrate produced by etching, taking advantage of the high thermal conductivity and low heat capacity at low temperatures of this material. A 150 nm CuNi heater (with temperature independent resistivity at 1 to 20 K) and a 150 nm NbN thermometer (with slope $\mathrm{d}R/R\,\mathrm{d}T \approx 0.2\,\mathrm{K}$ at 4 K) are deposited onto the substrate. The heat capacity of this addenda in the different versions of these calorimeters varied between less than $0.1\,\mathrm{nJ\,K^{-1}}$ at $T < 1\,\mathrm{K}$ and some $\mathrm{nJ\,K^{-1}}$ at 4 K. The device was used to measure heat capacities of systems of reduced dimensionality like deposited thin films or multilayers or of microgram single crystals and eventually of mesoscopic superconducting loops. The achieved resolution of $\Delta C/C < 5 \times 10^{-5}$ allowed measurements of variations of C as small as $10\,\mathrm{fJ\,K^{-1}}$ [3.68].

Another remarkable achievement reported in [3.70] seems to be the substantial improvement of the conventional differential thermal-analysis (DTA) method by means of using high-precision electronics and careful temperature control. This device was used to measure the heat capacity of milligram samples at Kelvin temperatures and in magnetic fields up to 7 T with a relative accuracy of about 10^{-4}. This makes this method particularly valuable for the investigation of sharp or shallow features at phase transitions. The main ingredient of the method is the continuous comparison of the heat capacity of the sample to the heat capacity of a reference material, which are both weakly connected to a thermal bath and which are simultaneously heated or cooled. The best results with this comparative method are, of course, achieved if thermal links and thermometers are as identical as possible. Temperature differences between bath, reference material, and sample are recorded and inserted in the relevant equations to evaluate the heat capacity of the sample.

An automated heat-capacity measurement system ("Physical Property Measurement System", see "Supplier of Cryogenic Equipment") for samples of about 10–500 mg is available commercially [3.64]. The system also allows performing very sensitive AC-susceptibility, as well as AC- and DC-magnetization and -electric-transport measurements. It employs the thermal relaxation method in the temperature range 1.8–400 K (optional 0.35–350 K with a continuously operating closed-cycle ^{3}He system; see Sect. 6.2). As an option, it can be equipped for measurements in magnetic fields up to 16 T longitudinal or 7 T transverse. Its calorimeter platform consists of a thin alumina square of 3×3 mm^2, backed by a thin-film heater and a bare Cernox thermometer (see Sect. 12.5.3). A heat pulse of duration τ is applied and the platform temperature is recorded for 2τ. With known values for the conductance of the thermal link to the bath, of the heat capacity of the addendum, and of the applied heat, the heat capacity of the sample and the internal time constant of the calorimeter are determined analytically from the T(t) data by numerically integrating the relevant differential equations. The curve fitting is improved by carrying out a number of decay sweeps at each temperature and averaging the results. Two Cernox thermometers are used over the full temperature range and their calibration is based on the ITS-90 temperature scale (Sect. 11.2). The resolution of the system is 10 nJ K^{-1} at 2 K. According to an examination of the system [3.64], the accuracy is 1% at 100–300 K, which diminishes to about 3–5% at $T < 5$ K. The system is quite adequate to investigate reasonably broad second-order phase transitions. However, sharp first-order transitions cannot be investigated properly, mainly because the applied software cannot describe the then non-exponential decay curves. This drawback can be removed by using an alternate analytic approach [3.64]. The system has recently been equipped with a simple, fully automated dilution refrigerator for heat-capacity measurements from 55 mK to 4 K and in fields to 9 T [3.71].

Important new information can be obtained from measurements of the angular dependence of the heat capacity in high magnetic fields. For example,

field-angle-dependent specific heat can probe the gap structure in unconventional superconductors such as high-T_c or heavy-fermion superconductors, possibly indicating the nodal structure of anisotropic energy gaps, which is intimately related to the pairing interaction [3.73]. In Sect. 13.7, I will describe various methods how to achieve the necessary rotation of samples at low temperatures in these fields.

Cryogenic calorimeters or more generally devices which measure the temperature increase after a deposition of energy are nowadays not only used to measure heat capacities of liquids and solids but also in a variety of other applications like the detection of weakly interacting massive particles, of x-rays and γ-rays, and in astrophysics; or as bolometers for detection of phonons, of particles or of electromagnetic waves, and in particular for detection of infrared radiation. These applications have emerged from the very high sensitivity of recent microcalorimeters in the range of nJ/K (corresponding to the heat capacity of a monolayer of ^{4}He, for example) or even less. For a recent review on these devices and their applications see [3.74].

3.2 Thermal Expansion

3.2.1 Thermal Expansion of Solids

If the potential which an atom sees in a crystal were parabolic (the harmonic approximation) and therefore given by (3.1), there would be no thermal expansion. However, in reality the potential which an atom experiences is anharmonic due to the electrostatic forces of its neighbours and looks more like that displayed in Fig. 3.16. At low temperatures the amplitudes of the atomic vibrations around their equilibrium position r_0 are rather small and the potential can be approximated by (3.1). As a result the thermal expansion coefficient

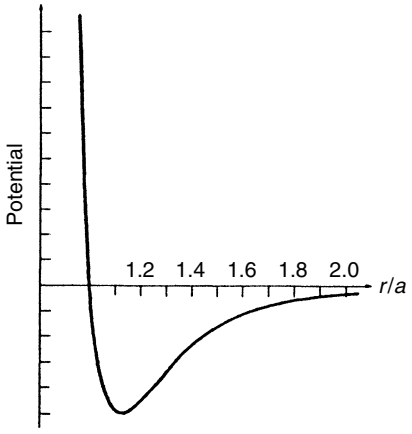

Fig. 3.16. Typical potential which an atom or ion experiences in a lattice as a function of distance r between them (normalized to the lattice parameter a)

$$\alpha = \frac{1}{l}\left[\frac{\partial l}{\partial T}\right]_p \tag{3.22}$$

does indeed vanish for $T \to 0$ (for Cu: $\alpha = 2.9 \times 10^{-10}T + 2.68 \times 10^{-11}T^3$ at $0.2\,\mathrm{K} < T < 1.9\,\mathrm{K}$ [3.75]).[2] When the temperature is raised the thermal vibrations of the atoms grow and they increasingly experience that the potential is asymmetric: steeper for small distances and flatter for larger distances. The atoms experience the "anharmonic" part of the potential. Due to the shape of the potential the atoms spend more of their time at larger separations, leading to an increased average separation. Therefore the material expands when the temperature is increased. For a potential $V(r - r_0) = V(x)$, the mean deviation from the zero-temperature position $r = r_0$ is given by [3.1–3.7]

$$\langle x \rangle = \frac{\int_{-\infty}^{+\infty} x \mathrm{e}^{-V(x)/k_\mathrm{B}T}\mathrm{d}x}{\int_{-\infty}^{+\infty} \mathrm{e}^{-V(x)/k_\mathrm{B}T}\mathrm{d}x}\,. \tag{3.23}$$

The thermal contraction of various materials when cooled from room temperature to lower temperatures is displayed in Fig. 3.17. Looking at this figure we can divide the materials quite generally into three groups. First, there is a group of commercial alloys and glasses, which have been specially produced to exhibit an extremely small expansion coefficient. Then we have the groups of metals which contract by about 0.2–0.4% when cooled from room temperature to low temperatures. It is very important to remember that different metals have different expansion coefficients and therefore have to be joined in the proper order (see below). Finally, we have the organic materials with their large expansion coefficients; typically 1–2% length change when cooled from room temperature to the low Kelvin temperature range. These latter materials are rather important for low-temperature purposes as well, because they are used as construction materials on account of their low thermal conductivity, or for bonding, electrical insulation or making leak-tight joints. Here problems can often occur due to their rather large thermal expansion coefficients which can lead to substantial thermal stresses. For some applications the very small expansion coefficients of many glasses of $\alpha \simeq 4 \times 10^{-7}\,\mathrm{K}^{-1}$ at 0°C may be useful. However, unlike the specific heat and other properties, α is not a universal property of glasses at low temperature; it may even have different sign for different glasses at $T \leq 1\,\mathrm{K}$ [3.81].

Joining materials of different thermal expansion in an apparatus whose temperature will repeatedly be changed requires a rather careful selection of the materials and a suitable design, if destruction of the joint by the severe stresses in thermal cycling is to be avoided. This is a very serious consideration because a low-temperature apparatus composed of a variety of materials usually has to be leak-tight. Figure 3.18 illustrates the correct ways of joining tubes of different

[2] Of course, when a material is anisotropic, it may have different expansion coefficients α_i in different directions. The volume expansion coefficient is then $\beta = \sum_{i=1}^{3} \alpha_i/3$.

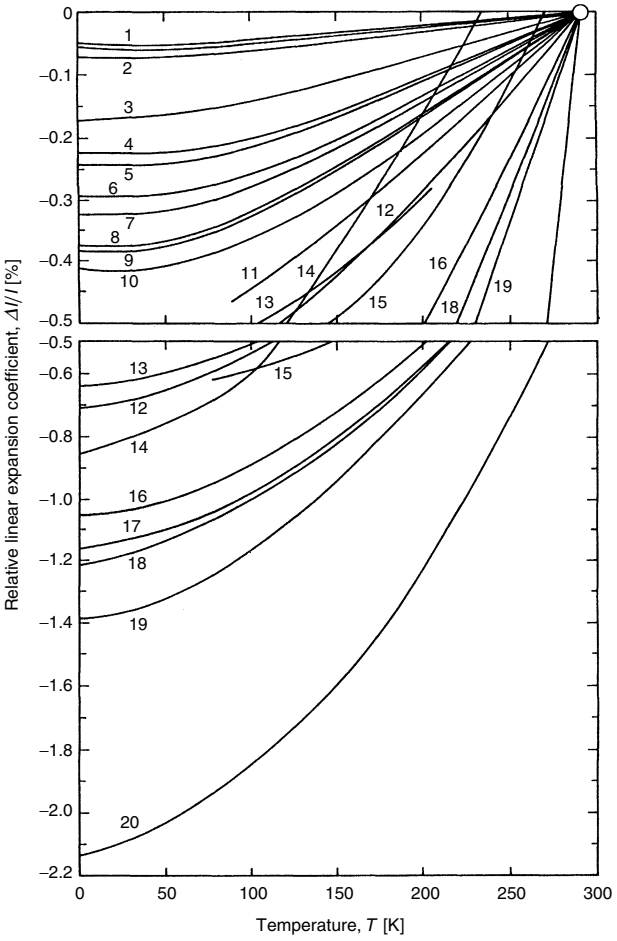

Fig. 3.17. Relative linear thermal expansion coefficient of (1) Invar (upper), Pyrex (lower), (2) W, (3) nonalloyed steel, (4) Ni, (5) $Cu_{0.7}Ni_{0.3}$, (6) stainless steel, (7) Cu, (8) German silver, (9) brass, (10) Al, (11) soft solder, (12) In, (13) Vespel SP22, (14) Hg, (15) ice, (16) Araldite, (17) Stycast 1266, (18) PMMA, (19) Nylon, (20) Teflon [3.76]. Some further data are: Pt similar to (3); Ag between (9) and (10); Stycast 2850 GT slightly larger than (10). The relative change of length between 300 and 4 K is $10^3 \Delta l/l = 12, 11.5, 4.4, 6.3$ and 5.7 for Polypropylene, Stycast 1266, Stycast 2850 GT as well as 2850 FT, Vespel SP-22 and solders, respectively [3.44, 3.55, 3.56, 3.76–3.82, 3.114]. Torlon behaves very similar to Stycast 2850FT [3.114]

metals and the design of seals, which appear in almost every piece of low-temperature equipment. (For the proper design of an insulating feedthrough of leads, see Sect. 13.3.) In addition, stresses due to parallel connection by parts of different materials have to be avoided. Very often good thermal contact between different metallic parts of low-temperature apparatus is essential

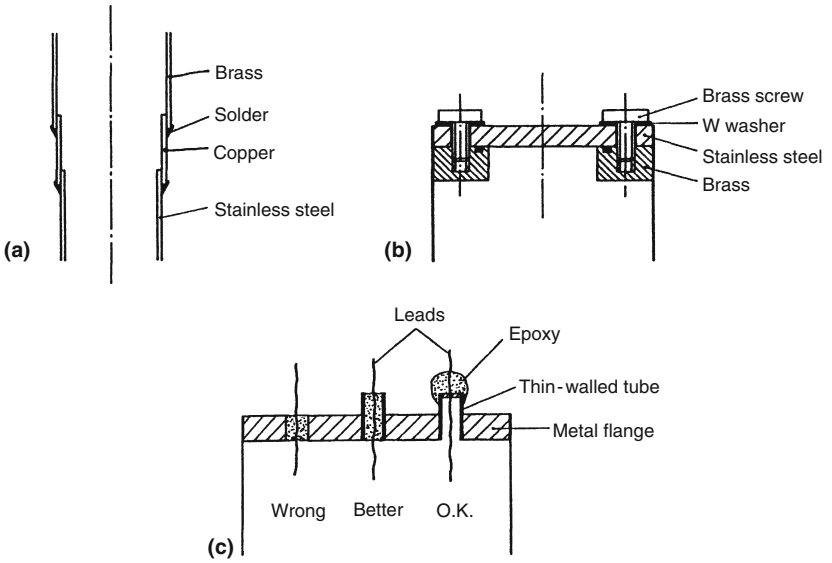

Fig. 3.18. When joining different materials in a cryogenic apparatus one has to take into account the difference in their thermal expansion coefficients. For example: (**a**) The tube with the largest expansion coefficient should be on the outside so that the solder joint is not pulled open during cooldown. (**b**) In an O-ring seal the screw should have a larger expansion coefficient than the flange. The seal will tighten even further during cooldown if a washer with a very small expansion coefficient is used. (**c**) In an epoxy feedthrough for leads the epoxy, with its large expansion coefficient, should contract on a thin-walled metal tube during cooldown rather than pull away. It helps if the tube walls are tapered to a sharp edge. An epoxy with filler should be used to lower its thermal expansion coefficient

(Sect. 4.3.1). Here again the correct selection of the materials for bolts and nuts is important. Frequently, the thermal contact after cooldown can be improved by adding a washer of a material with a low thermal expansion coefficient, such as Mo or W (but they are superconductors at very low temperatures!).

A fairly comprehensive list of references and data on thermal expansion coefficients of solids can be found in [3.7, 3.44, 3.78–3.80].

3.2.2 Dilatometers or How to Measure Thermal Expansions

For measurements of thermal expansion coefficients, capacitive displacement sensors are commonly used because of their sensitivity (up to 0.1 nm) and simplicity (see also Sect. 13.1) [3.7, 3.78, 3.79, 3.82]. In these dilatometers, the change of length of a sample is transferred to the movable part of a capacitor resulting in a capacitance change. The capacitances are measured in a five-terminal capacitance bridge like the one discussed in Sect. 13.1.1 or in a commercial high-resolution capacitance bridge. The resolution of these bridges of up to 10^{-7} or even 10^{-8} translates to resolution changes of up to 0.1 nm.

A miniature capacitance dilatometer of this type with only 22 mm diameter, made from Ag and suitable for measuring thermal expansion and magnetostriction of small and irregularly shaped samples even in very high magnetic fields has been described in [3.83]. The design is based on the tilted-plane technique, so that the problem of holding the capacitor plates parallel to each other is overcome. Its resolution is 0.1 nm or Δl/l=10^{-6} and it has been used in a cryostat inside of the narrow (32 mm) and "noisy" bore of a magnet with fields up to $33\,T$. For earlier designs using capacitive dilatometers, the mentioned publications should be consulted.

Capacitance dilatometers are only surpassed by dilatometers using a SQUID as the sensing element of elongation or contraction of a sample. The enormous resolution of 2×10^{-5} nm has been achieved and the data for Cu at $0.2 < \mathrm{T} < 1.9\,\mathrm{K}$, mentioned above, have been obtained applying such a device [3.75].

3.3 Thermal Conductivity

Thermal conductivity is a transport property of matter similar to electrical conductivity, viscosity, diffusion, damping of sound, etc [3.1–3.6, 3.84–3.87]. The rate of heat flow per unit area resulting from a temperature gradient in a material of cross-section A is given by

$$\dot{q} = \dot{Q}/A = -\kappa \nabla T\,, \tag{3.24}$$

where κ is the thermal conductivity coefficient. Heat can be carried by conduction electrons or by lattice vibrations; their contributions are additive. These carriers of heat usually do not fly ballistically from the heated end of the material to the other colder end. They are scattered by other electrons or phonons or by defects in the material; therefore they perform a diffusion process. To calculate thermal transport we have to apply transport theory, which in its simplest form is a kinetic gas theory. In this simplified version we consider the electrons or the phonons as a gas diffusing through the material. For the thermal conductivity coefficient this theory gives

$$\kappa = \frac{1}{3}\frac{C}{V_\mathrm{m}} v \lambda\,, \tag{3.25}$$

where λ is the mean free path, and v is the velocity of the particles. Intuitively, this is a rather convincing equation identical to those for other transport properties if we choose the corresponding parameters. It tells us that the transport property "thermal conductivity coefficient" is given by the product of "what is transported" [here it is the specific heat C (per unit volume)], "the velocity v of the carriers performing the transport", and "how far the carriers fly before they are scattered again". The factor 1/3 comes from the fact that we are interested in the heat flow in one direction, whereas the motion of the carriers is three-dimensional.

How will the thermal conductivity coefficient look like if the heat is carried by the electron or/and by the phonon gases? In the first part of this chapter we have already calculated the specific heat C of electrons and phonons as a function of temperature. The characteristic velocity of phonons is the velocity of the sound v_s; this is the velocity with which "vibrations" or "phonons" move through the lattice. Typical values for solids, in particular metals, are $v_s = (3\text{–}5) \times 10^5\,\mathrm{cm\,s^{-1}}$. The electrons involved in thermal transport can only be electrons with energy near the Fermi energy (Fig. 3.3). Only these can transport heat because they are the only ones which can perform transitions to higher nonoccupied energy states, which is necessary for thermal conductivity. Their velocity is the so-called Fermi velocity v_F determined by the kinetic Fermi energy E_F, see (3.10). Typical values for

$$v_F = (\hbar/m_e)(3\pi^2 N_0/V_m)^{1/3} \tag{3.26}$$

are 10^7–$10^8\,\mathrm{cm\,s^{-1}} \gg v_s$. Both the sound velocity and the Fermi velocity are independent of temperature at low temperatures. So we know C and v, and all the problems in calculating transport properties lie in the calculation of the mean free path λ, determined by the scattering processes of the heat carriers.

The main scattering processes limiting the thermal conductivity are phonon–phonon (which is absent in the harmonic approximation), phonon–defect, electron–phonon, electron–impurity, and sometimes electron–electron interactions. The latter process is rather ineffective because it involves four different electron states due to the Pauli exclusion principle. The resistances of the various scattering processes are additive. Because the number of phonons increases with increasing temperature, the electron–phonon and phonon–phonon scattering rates are temperature dependent. The number of defects is temperature independent and correspondingly the mean free path for the phonon–defect and electron–defect scattering do not depend on temperature. As a result, we arrive at the equations for the thermal conductivity given in the following subsections.

3.3.1 Lattice Conductivity: Phonons

The lattice or phonon conductivity which is the dominant and mostly the only conduction mechanism in insulators is given by

$$\kappa_{ph} = \frac{1}{3}\frac{C_{ph}}{V_m} v_s \lambda_{ph} \propto T^3 \lambda_{ph}(T), \quad \text{at } T \le \theta_D/10\,. \tag{3.27}$$

Intermediate Temperatures: $T \le \theta_D/10$

In this temperature range the phonon–phonon scattering is dominant and the phonon mean free path increases with decreasing temperature because

the number of phonons decreases with decreasing temperature. A quantitative derivation [3.1–3.6, 3.84–3.87] of the thermal conductivity for the phonon–phonon scattering regime is somewhat involved due to the anharmonicity of the potential and of the frequency dependence of the dominant phonons with temperature; it will not be given here. We just state that in this T range the thermal conductivity decreases with increasing temperature (Figs. 3.19 and 3.20).

Low Temperatures: $T \ll \theta_D$

In this temperature range the number of thermally excited phonons is rather small. They are no longer important for scattering, and the phonons which carry the heat are scattered by crystal defects or by crystal boundaries only. Because at low temperatures the dominant phonon wavelength is larger than the size of the lattice imperfections, phonon scattering at crystallite boundaries is the important process. Now the mean free path for phonon transport is, in general, temperature-independent – but see (3.29). The temperature dependence of the thermal conductivity is then given just by the temperature dependence of the specific heat, and decreases strongly with decreasing temperature as

$$\kappa_{\mathrm{ph}} \propto C_{\mathrm{ph}} \propto T^3 \,. \tag{3.28}$$

As a result of this consideration we find that the thermal conductivity due to phonon transport goes through a maximum, as illustrated in Figs. 3.19a and 3.20. Owing to differences in the number of defects, the low temperature thermal conductivity of nominally identical samples can vary considerably (see also Fig. 3.19).

I want to mention two particularly important cases of phonon thermal conductivity. First, if we have a rather perfect, large crystal with a very low density of defects and impurities, the mean free path of phonons and therefore the thermal conductivity can become very large, of the order 100 W (cm K)$^{-1}$ (Figs. 3.19a and 3.20). This is comparable to the thermal conductivity of highly conductive metals like copper or aluminum. Second, if we have a strongly disordered insulator, the mean free path determined by the scattering of phonons on defects can become very small, even approaching atomic distances. In particular, if we consider a glass, the tunneling transitions between different structural arrangements of the atoms, which were discussed in the description of the specific heat of noncrystalline materials (Sect. 3.1.4), limit the phonon thermal conductivity by additional scattering of phonons on tunneling states [3.5, 3.24–3.28, 3.94, 3.95]. They reduce the thermal conductivity of glasses considerably, for example by about two (four) orders of magnitude for vitreous silica compared to crystalline quartz at 1 (10 K) [3.27]. This scattering results in an almost universal close to T^2 dependence of the thermal conductivity of dielectric glassy materials below 1 K (Figs. 3.21–3.23) and

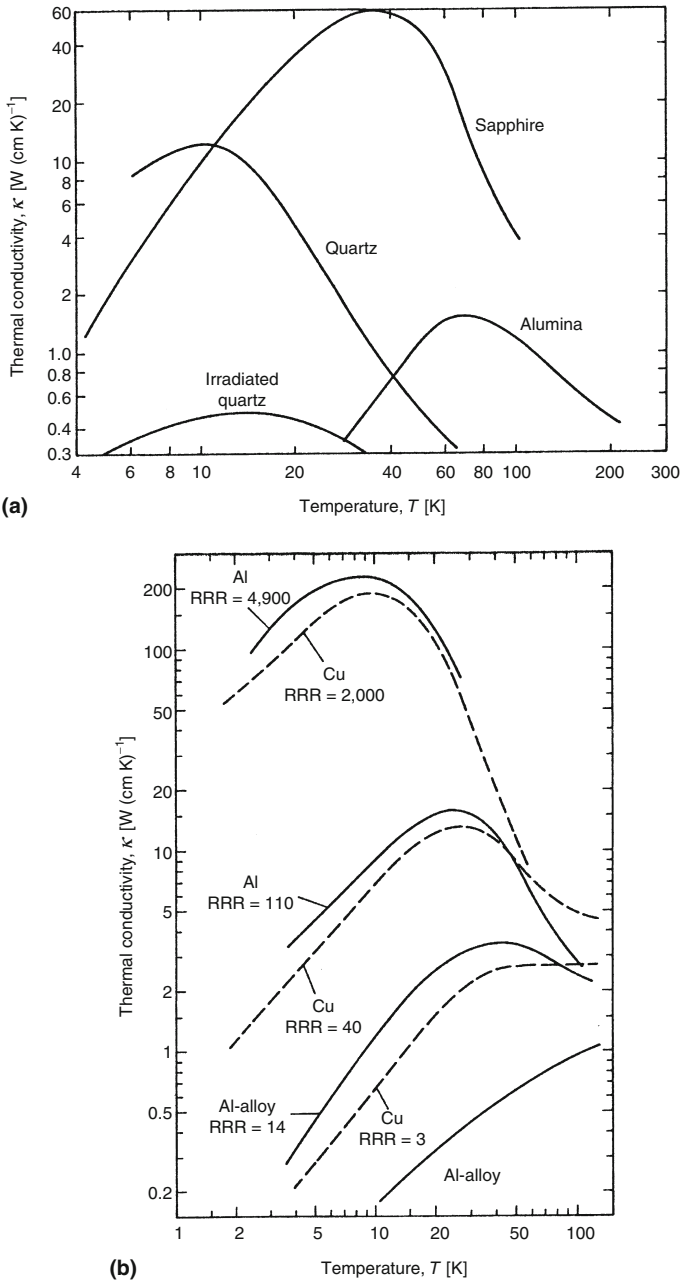

Fig. 3.19. Temperature dependence of the thermal conductivities of (**a**) some dielectric solids and of (**b**) Al and Cu of varying purity [expressed as their residual resistivity ratio (3.43)] [3.88]

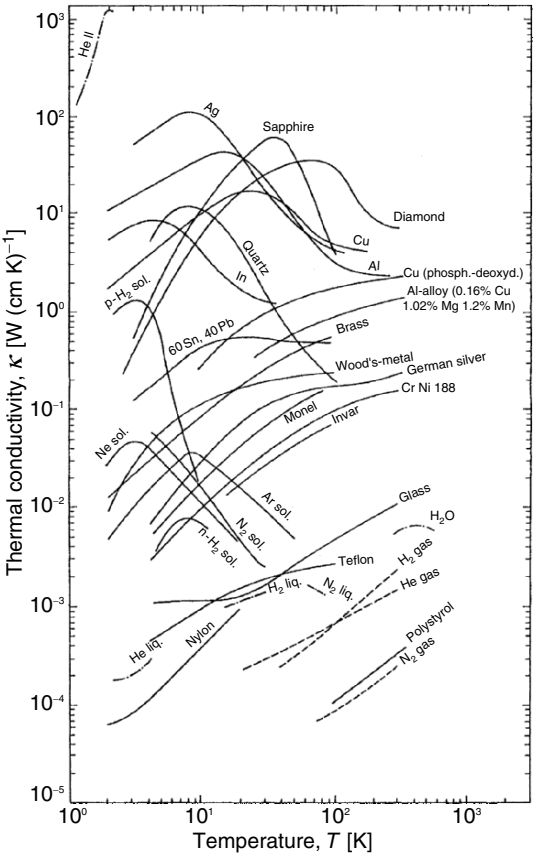

Fig. 3.20. Typical thermal conductivities κ of various materials at $T > 2\,\mathrm{K}$ [3.89–3.93]. Remember that κ depends on the purity and crystalline perfection of a material

a plateau region for $2\,\mathrm{K} \lesssim T \lesssim 20\,\mathrm{K}$ (Fig. 3.22). Because the heat is still carried by phonons with $C_{\mathrm{ph}} \propto T^3$, the phonon mean-free path limited by scattering on tunneling states must vary as $\lambda \propto T^{-1}$. As for the specific heat of disordered solids, both the absolute magnitude and the temperature dependence of the thermal conductivities of most glasses are rather similar; for example, for commercial glasses or polymers they fall within about a factor of two of those given for Pyrex (Figs. 3.21 and 3.22).

A detailed discussion of the lattice conductivity is rather involved due to the variation of the frequency of the dominant phonons with temperature and the various scattering processes. This is particularly true if the conductivity is limited by different lattice imperfections. The main results of such discussions are [3.1–3.6, 3.84, 3.86].

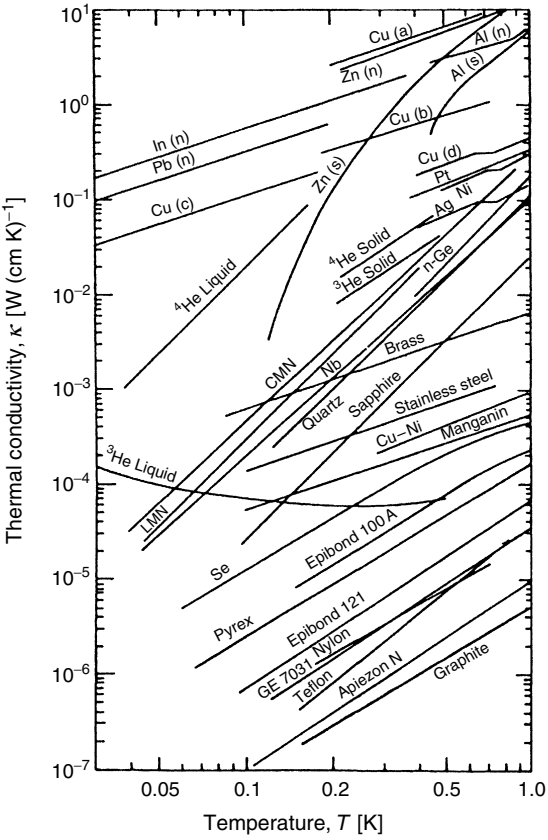

Fig. 3.21. Typical thermal conductivities κ of various materials at $T < 1\,K$ [3.45]. (This publication provides references to the original literature.) Remember that κ depends on the purity and crystalline perfection of a material

$$\begin{aligned} &\lambda_{\mathrm{ph}} = \text{const.} \quad \text{for phonon–grain boundary scattering,} \\ &\lambda_{\mathrm{ph}} \propto T^{-1} \quad \text{for phonon–dislocation scattering, and} \\ &\lambda_{\mathrm{ph}} \propto T^{-4} \quad \text{for phonon–point defect (Rayleigh) scattering.} \end{aligned} \tag{3.29}$$

3.3.2 Electronic Thermal Conductivity

For the thermal conductivity due to conduction electrons we have

$$\kappa_{\mathrm{e}} = \frac{1}{3}\frac{C_{\mathrm{e}}}{V_{\mathrm{m}}} v_{\mathrm{F}} \lambda_{\mathrm{e}} \propto T \lambda_{\mathrm{e}}(T)\,. \tag{3.30}$$

Usually, in a metal, this electronic thermal conductivity is considerably larger than the lattice thermal conductivity because the Fermi velocity v_{F} of

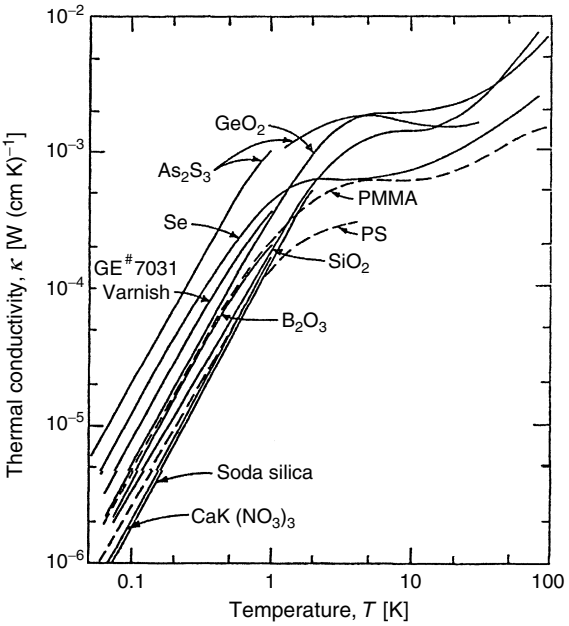

Fig. 3.22. Thermal conductivities of various noncrystalline solids [3.28]. For recent data on the glass BK 7 and Corning No. 2 coverglass between 6 and 700 mK see [3.96,3.97]; they are 0.2 to 0.3 mW cm^{-1} K^{-1} at 1 K and with a temperature dependence of about $T^{1.85}$. For more data on amorphous materials see Table 3.2

the conduction electrons is much larger than the sound velocity v_s of phonons. A detailed theoretical treatment [3.1–3.6, 3.84–3.87] of the electronic thermal conductivity is easier than that of the lattice conductivity because the conduction electrons involved sit within a narrow energy band of width $k_B T$ at the Fermi energy E_F and therefore they all have the same energy.

High Temperatures

At high temperatures the thermally excited phonons are the limiting scatterers for the heat conducting electrons. Because the number of thermally excited phonons increases with temperature we find for the electronic thermal conductivity in the electron–phonon scattering region a thermal conductivity which decreases with increasing temperature (Figs. 3.19b and 3.20).

Low Temperatures

At low temperatures the number of phonons is again small and the scattering of electrons from lattice defects and impurities dominates. We have a

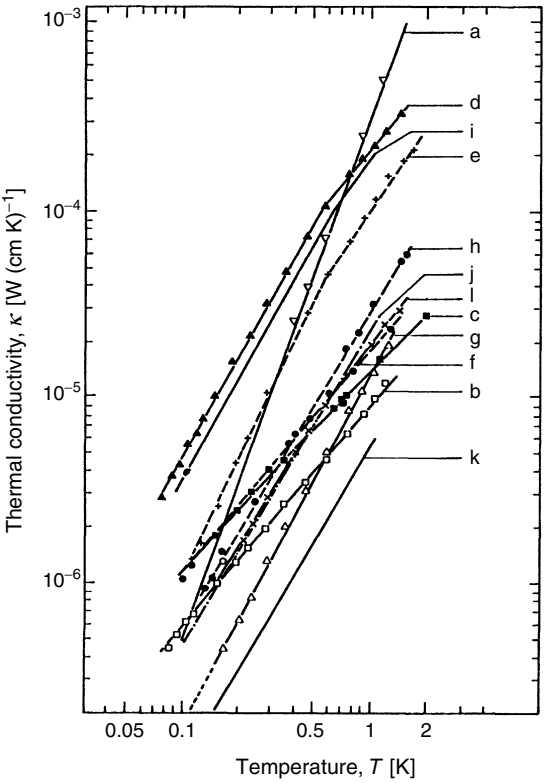

Fig. 3.23. Thermal conductivities of various dielectric materials often used in a cryogenic apparatus (a, sintered Al_2O_3; b, carbon BB5, c, nuclear graphite; d, Araldite CT 200; e, Araldite with talc; f, Vespel SP1; g, Vespel SP22; h, Vespel SP5; i, Epibond 100 A; j, Nylon; k, Graphite AGOT; l, Vespel SP21 with 15% by weight graphite) [3.94]

temperature-independent electronic mean free path resulting in the following equation for the electronic thermal conductivity:

$$\kappa_e \propto C_e \propto T\,. \tag{3.31}$$

We again have two scattering processes dominating in different temperature regions and with opposite temperature dependences. As a result the electronic contribution to the thermal conductivity also goes through a maximum (Figs. 3.19b and 3.20). The value and position of this maximum strongly depend on the perfection of the metal; for pure elements it is located at about 10 K. With increasing impurity concentration, the maximum is diminished and shifted to higher temperature. In a disordered alloy the scattering of electrons by the varying potential can become so strong that electronic and lattice conductivities become comparable.

3.3.3 Thermal Conductivity at Low Temperatures

For our purposes the values and temperature dependences of the thermal conductivity at low temperatures are of particular importance and will be summarized in the following. The heat carried by a material of cross-section A and length L with a thermal conductivity coefficient κ and with temperatures. T_2 and T_1 at its ends is given by

$$\dot{Q} = \frac{A}{L}\int_0^L \dot{q}\,\mathrm{d}x = \frac{A}{L}\int_{T_1}^{T_2} \kappa(T)\mathrm{d}T\,. \tag{3.32}$$

Insulators/Phonons

Here we have

$$\kappa_{\mathrm{ph}} = bT^3 \quad \text{for } T < \theta_{\mathrm{D}}/10 \tag{3.33}$$

and hence

$$\dot{Q} = \frac{Ab}{4L}(T_2^4 - T_1^4)\,. \tag{3.34}$$

For small temperature gradients, $\Delta T = T_2 - T_1 \ll T$, we have

$$\dot{Q} \simeq \frac{Ab}{L}T^3\Delta T = \frac{A}{L}\kappa_{\mathrm{ph}}(T)\Delta T\,. \tag{3.35}$$

Metals/Conduction Electrons

Here we have

$$\kappa_{\mathrm{e}} = \kappa_0 T \quad \text{for } T < 10\,K \tag{3.36}$$

and therefore

$$\dot{Q} = \frac{A\kappa_0}{2L}(T_2^2 - T_1^2)\,. \tag{3.37}$$

Again, for small temperature gradients,

$$\dot{Q} \simeq \frac{A\kappa_0}{L}T\Delta T = \frac{A}{L}\kappa_{\mathrm{e}}(T)\Delta T\,. \tag{3.38}$$

Hence, an accurate determination of thermal conductivity involves also an accurate determination of the relevant sample dimensions.

Low-temperature thermal conductivities of various materials are listed in Table 3.2 and plotted in Figs. 3.19–3.23.

Table 3.2. Thermal conductivity of solids frequently used in low temperature apparatus

material	κ [mW (cm K)$^{-1}$]	T range [K]	ref.
Manganin	$0.94\ T^{1.2}$	1–4	[3.98]
Nb–Ti	$0.075\ T^{1.85}$	4–9	[3.99]
Nb–Ti	$0.15–0.27\ T^{2.0}$	0.1–1	[3.100]
$Cu_{0.70}Ni_{0.30}$	$0.93\ T^{1.23}$	0.3–4	[3.101]
$Cu_{0.70}Ni_{0.30}$	$0.64\ T$	0.05–3.0	[3.100, 3.102]
Pyrex	$0.15\ T^{1.75}$	0.18–0.8	[3.103]
Al_2O_3	$2.7\ T^{2.5}$	2–8	[3.104]
Al_2O_3	$0.29\ T^{2.7}$	0.1–2	[3.94]
Stycast 1266	$0.49\ T^{1.98}$	0.05–0.5	[3.105]
Stycast 1266	$0.39\ T^{1.9}$	0.06–1	[3.100]
Stycast 2850 GT	$78 \times 10^{-3}\ T^{1.8}$	1–4	[3.98]
Stycast 2850 FT	$53 \times 10^{-3}\ T^{1.8}$	2–10	[3.106]
Stycast 2850 FT	$92 \times 10^{-3}\ T^{2.65}$	0.06–1	[3.100]
Vespel SP 1	$18 \times 10^{-3}\ T^{1.2}$	0.1–1	[3.94]
Vespel SP 22	$17 \times 10^{-3}\ T^{2}$	0.1–2	[3.94, 3.100]
Teflon	$30 \times 10^{-3}\ T^{2}$	0.2–1	[3.107]
Teflon	$38 \times 10^{-3}\ T^{2.4}$	0.3–0.7	[3.103]
Nylon	$26 \times 10^{-3}\ T^{1.75}$	0.2–1	[3.94, 3.103]
Macor	$58 \times 10^{-3}\ T^{2.24}$	0.4–1.1	[3.108]
Nuclear graphite	$15 \times 10^{-3}\ T^{1.13}$	0.1–2	[3.94]
AGOT graphite	$5.1 \times 10^{-3}\ T^{1.76}$	0.1–2	[3.94]
	$4.9 \times 10^{-3}\ T^{1.86}$	0.3–3	[3.109]
a-SiO_2	$0.248\ T^{1.91}$	0.06–1	[3.110]
Wood	$9.3 \times 10^{-3}\ T^{2.7}$	0.04–1	[3.111]
Kevlar	$3.9 \times 10^{-5}\ T^{1.17}$	0.1–2.5	[3.112]
Polypropylene	$27.4 \times 10^{-3}\ \mathrm{T}^{1.28}$	0.1–1	[3.56]
PVC	$1.8 \times 10^{-4}\ \mathrm{T}^{2.05}$	0.05–0.12	[3.113]
Torlon	$6.13 \times 10^{-2}\ \mathrm{T}^{2.18}$	0.1–0.8	[3.114]

The given temperature ranges are the ranges where the given equations describe the data; in the cited literature, often data for a much wider temperature range are given.

3.3.4 Superconducting Metals

In superconducting metals some of the electrons are paired to so-called Cooper pairs. They all sit in the same low energy state of zero entropy, which is separated by an energy gap ΔE from the states of the single, unpaired electrons [3.16–3.19, 3.23]. The Cooper pairs cannot leave this ground state to carry heat (they carry no entropy) unless they are broken up into single electrons. Therefore in a superconducting metal only the remaining unpaired electrons can carry heat. Because they are in energy states which are separated from the Cooper ground state by the energy gap $\Delta E(T)$, their

number decreases exponentially with T, i.e., as $\exp(-\Delta E/k_{\mathrm{B}}T)$. As a result of this qualitative discussion we find that the electronic thermal conductivity of a metal in the superconducting state is given by the product of the number of remaining unpaired single electrons and their thermal conductivity (which is identical to the electronic thermal conductivity $\kappa_{\mathrm{e,n}} = \kappa_0\ T$ in the normal–conducting state),

$$\kappa_{\mathrm{e,s}} \propto T\mathrm{e}^{-\Delta E/k_{\mathrm{B}}T}\,, \tag{3.39}$$

with $\Delta E = 1.76 k_{\mathrm{B}} T_{\mathrm{c}}$ for most elemental superconductors [3.16–3.19, 3.23].

Hence, the electronic thermal conductivity of a superconductor decreases very rapidly with decreasing temperature [3.115]. Indeed, at low temperatures the electronic thermal conductivity of a superconducting metal can even become smaller than its lattice conductivity, and at sufficiently low temperatures, say at $T < T_{\mathrm{c}}/10$, the total thermal conductivity of a superconductor approaches the thermal conductivity of an insulator, $\kappa \propto T^3$. This is shown in Fig. 4.1 for aluminium.

Because it is rather simple to "switch" a metal from the superconducting to the normal state by applying a large enough magnetic field, one can "switch" its thermal conductivity from one state to the other. We take advantage of this possibility by using a superconducting metal as a thermal switch to disconnect or to connect two parts in a low-temperature apparatus, for example in a magnetic refrigerator (Chap. 10). This application will be discussed in Sect. 4.2.2.

3.3.5 Relation Between Thermal and Electrical Conductivity: The Wiedemann–Franz Law

A correct measurement of the low-temperature thermal conductivity of a metal can be rather cumbersome (see Sect. 3.3.7) and, in general, a measurement of the electrical conductivity is much easier. Fortunately, due to the fact that in a metal usually both conductivities are determined by the flow of electrons and are mostly limited by the same scattering processes, a measurement of the electrical conductivity often gives reasonable information about the thermal conductivity. Let us consider a metal at low temperatures in the defect scattering limit where $\lambda_{\mathrm{e}} = \mathrm{const}$. For the electrical conductivity the electrons conduct charge, which is temperature independent. At low temperatures in the defect scattering limit or in the residual resistivity range (see below) the electrical conductivity σ is therefore temperature independent. For the thermal conductivity κ the electrons carry heat, but the specific heat, and therefore the thermal conductivity, are proportional to temperature in this range. As a result, the ratio of thermal conductivity κ to electrical conductivity σ is proportional to temperature. One arrives at the same result for the temperature range where the conductivity due to electron transport is limited by large-angle elastic electron–phonon scattering ($T \geq \theta_{\mathrm{D}}$). At, say,

4 and 300 K, we then have the Wiedemann–Franz law for the ratio of these two conductivities [3.1–3.6, 3.84–3.87, 3.116],

$$\kappa/\sigma = L_0 T\,, \tag{3.40}$$

where the Lorenz number L_0 is a universal constant, i.e., $L_0 = (\pi\kappa_\mathrm{B}/e)^2/3 = 2.4453 \times 10^{-8}\,W\ \Omega\mathrm{K}^{-2}$.

Of course, we also arrive at (3.40) if we combine the equation for the electrical conductivity of a metal

$$\sigma = \frac{nN_0e^2\lambda_\mathrm{e}V_\mathrm{m}}{v_\mathrm{F}m^*}\,, \tag{3.41}$$

where m^* is the effective mass of the conduction electrons and n is the number of conduction electrons per atom, with (3.30) for the thermal conductivity, assuming that the electronic mean free path is the same for both conductivities.

We can therefore use the measured electrical conductivity together with the Wiedemann–Franz law to calculate the thermal conductivity. In many situations this gives correct results, in particular when the electron scattering is predominantly elastic. It most often holds at low temperatures (impurity scattering; $T < \theta/10$) and at high temperatures (phonon scattering; $T \geq \theta$) but not in between, where energy losses of the order $k_\mathrm{B}T$ are associated with electron–phonon collisions. However, cases are known in which the calculated and measured thermal conductivities differ by up to an order of magnitude at low temperatures. Usually the measured thermal conductivity is smaller than the thermal conductivity calculated with the Wiedemann–Franz law from the electrical conductivity. Particularly disturbing is the observation that this can happen at Kelvin and lower temperatures for metals of typical quality commonly used in a low-temperature apparatus (e.g., Al and Ag) while this deviation can be absent for other quite similar metals (e.g., Cu) [3.104], see Fig. 3.24, or has even not been observed for the same metal by other investigators [3.117, 3.118]. The reason for this discrepancy is the fact that our earlier discussion is an oversimplification. In reality scattering processes may contribute with different "effectiveness" to the two conductivities, in particular when inelastic scattering contributes to the thermal conductivity [3.1–3.6, 3.84–3.87].

A formula that is rather useful can be derived from the above equations, namely,

$$v_\mathrm{F}\lambda_\mathrm{e} = \frac{\sigma}{\gamma}\left[\frac{\pi k_\mathrm{B}}{e}\right]^2 \tag{3.42}$$

which allows the electronic mean free path λ_e to be calculated from the measured electrical conductivity σ and specific heat coefficient γ.

In the literature the so-called residual resistivity ratio (RRR) is very often given as a measure of the "purity" of a metal (Fig. 3.19). This is the ratio of the electrical conductivity at low temperatures, e.g., at the boiling point of liquid helium, to the electrical conductivity at room temperature

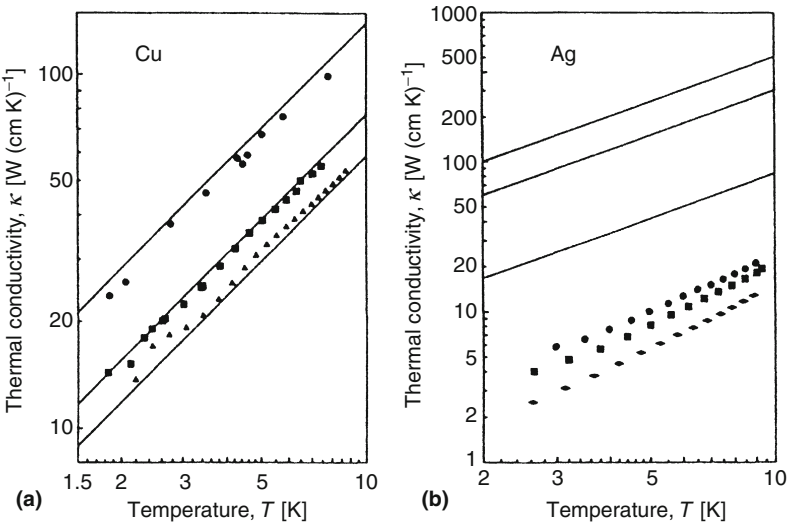

Fig. 3.24. (**a**) Thermal conductivity of a Cu foil 60 μm thick and 20 mm wide after various treatments, resulting in RRRs of 979 (●), 540 (■) and 410 (▲). Lines correspond to thermal conductivities calculated from RRR values (3.43) by applying the Wiedemann–Franz law (3.40). (**b**) Thermal conductivity of a Ag rod 0.86 × 0.86 mm^2 after different treatments, resulting in RRRs of 3,330 (●), 1,988 (■) and 553 (▲). Lines correspond to thermal conductivities calculated from RRR values (3.41) by applying the Wiedemann–Franz law (3.40). The shown results mean that different types of defects may influence the thermal and the electric conductivities differently. Hence, the results may differ from sample to sample [3.104]

$$\mathrm{RRR} = \sigma_{4.2\,\mathrm{K}}/\sigma_{300\,\mathrm{K}} = \rho_{300\,\mathrm{K}}/\rho_{4.2\,\mathrm{K}}\,. \tag{3.43}$$

Because the room-temperature conductivity is determined not by defect scattering but by phonon scattering, whereas the low-temperature conductivity is exclusively determined by the scattering on defects because then there are no phonons left – this ratio is a direct measure of the limiting defect scattering. It indicates how good a material is by stating by what factor its conductivity increases with the vanishing of the phonon scattering at low temperatures.

3.3.6 Influence of Impurities on Conductivity

In Sect. 3.3.5 we have discussed how the thermal conductivity – which is so important for low-temperature experiments – can be calculated from the electrical conductivity and that both conductivities are limited at low temperatures by electron–defect scattering in a metal. In this section I will make some comments on the scattering of conduction electrons on impurity atoms. For this scattering we have to distinguish between nonmagnetic and magnetic impurities.

Electron Scattering by Nonmagnetic Impurity Atoms

The conduction electrons are scattered at the Coulomb potential of the impurity, which may have the valence difference ΔZ compared to the host lattice. The increase of the electrical resistance in this case is often not very large, and for small impurity concentrations is given by the Linde rule

$$\Delta\rho_{\mathrm{nm}} = a + b(\Delta Z)^2 \,. \tag{3.44}$$

The constants a and b are determined by the host lattice and, in particular, depend on the row of the Periodic Table to which the host atom belongs. Examples for Cu as the host are listed in Table 3.3. These values are typically $1\,\mu\Omega\,\mathrm{cm}\,(\mathrm{at}\ \%)^{-1}$ (impurity concentration); they are comparable to the increase of ρ due to heavy cold working (several 10 $n\Omega\ cm$) or introduction of vacancies ($1\,\mu\Omega\,\mathrm{cm}\,(\mathrm{at}\ \%)^{-1}$) [3.45, 3.87].

Scattering of Electrons by Magnetic Impurity Atoms (in Particular in Copper)

A magnetic or spin-flip scattering of the conduction electrons can occur at localized moments of magnetic impurities [3.5, 3.119–3.121]. For this situation the increase of resistance can be much larger – and much more difficult to understand theoretically – than for the case of nonmagnetic impurities; a theoretical discussion and a calculation of $\Delta\rho_{\mathrm{m}}$ is much more involved. Examples for 3d elements as impurities in Cu are listed in Table 3.4. The strength of the scattering and the resulting resistance increase depend strongly on the properties of the magnetic impurity and it can be very different in different host lattices. For example, iron produces a very large moment of about $12\,\mu_{\mathrm{B}}$ in palladium [3.122], it keeps essentially its bare moment of about $2\,\mu_{\mathrm{B}}$ in noble metals, whereas its moment at low temperatures is very small in rhodium [3.123]

Table 3.3. Relative change $\Delta\rho_{\mathrm{nm}}$ per concentration c of the solute of the electrical resistance of Cu if the given nonmagnetic elements with valence difference ΔZ compared to Cu are introduced as impurities, see (3.44), [3.87]

impurity	As	Si	Ge	Ga	Mg	Zn	Cd	Ag
ΔZ	4	3	3	2	1	1	1	0
$\Delta\rho_{\mathrm{nm}}/c$ [$\mathrm{n\Omega\,cm\,(at.\ ppm)^{-1}}$]	0.65	0.33	0.37	0.14	0.065	0.025	0.02	0.014

Table 3.4. Relative change $\Delta\rho_{\mathrm{m}}$ per concentration c of the solute of the electrical resistance of Cu at 1 K if the given magnetic elements are introduced as impurities [3.87]

impurity	Ti	V	Cr	Mn	Fe	Co	Ni
$\Delta\rho_{\mathrm{m}}/c$ [$n\Omega\,\mathrm{cm\,(at.\ ppm)^{-1}}$]	1.0	0.58	2.0	0.43	1.5	0.58	0.11

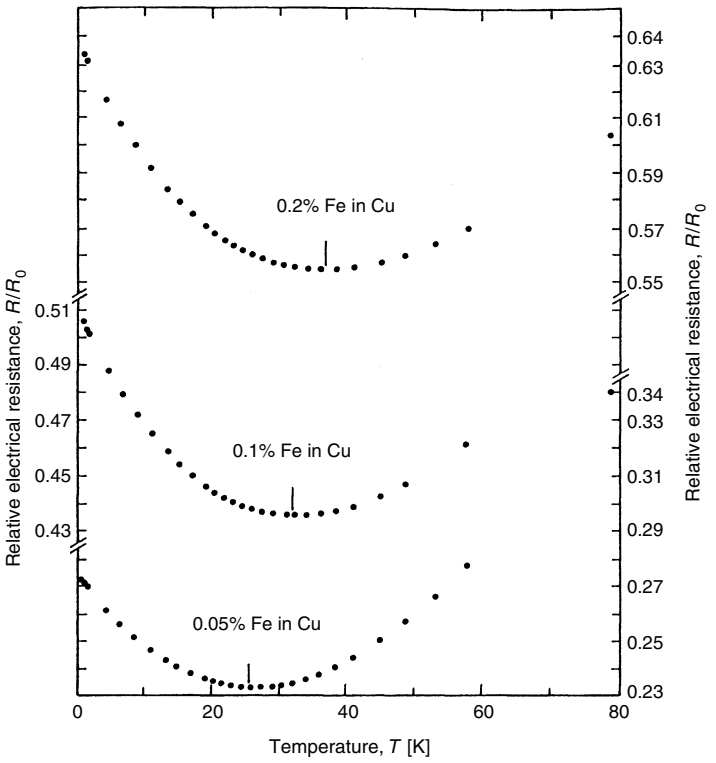

Fig. 3.25. Resistance minima of various dilute alloys of Fe in Cu. R_0 is the resistivity at 0°C. The position of the minimum depends on the concentration of iron [3.125]. For similar, more recent data for Fe in Au see [3.126]

or aluminum [3.124]. Hence, Fe has a strong impact on transport properties in noble and platinum metals, however almost no impact on them in Rh and Al. Furthermore, the strength of the scattering can depend very strongly on temperature due to the so-called Kondo effect, which describes an enhanced inelastic scattering of a cloud of conduction electrons "condensed" around magnetic moments that are localized on impurity atoms [3.5, 3.119–3.121]. The latter experience a temperature-dependent screening by the conduction electrons of the host lattice. As a result the resistivity may not approach a constant value ρ_0 at low temperatures but may rise logarithmically with decreasing temperature T after passing through a minimum whose position depends weakly on the concentration of the impurity (Fig. 3.25). It is then given by

$$\rho = \rho_0 - \rho_K \ \ln(T) \tag{3.45}$$

where ρ_K denotes the Kondo resistivity.

3.3.7 Thermal Conductivities of Copper, Silver and Aluminum at Low Temperatures

Aluminum and copper (and for some special applications, the more expensive silver; however, it usually contains a substantial amount of O_2) are the most widely used thermal conductors in a low-temperature apparatus. Aluminum has the advantages over Cu that it has a lower density, it is available in higher purity (up to 6 N, whereas Cu seems presently to be commercially available only up to 5 N), and in particular its conductivity is less dependent on deformation (it anneals already at room temperature) and on the amount of impurities (paramagnetic ions have a very small moment in Al opposite to their properties in Cu; see above). However, Cu (and Ag) has the advantage that it is easy to make good thermal contact to it which is much harder for Al due to its tenacious oxidized surface layer (see Sect. 4.2.2). For these metals, the thermal conductivities at low temperatures vary over many orders of magnitude depending on treatment and purity (Fig. 3.19). As a rule of thumb: their RRR is about equal to the thermal conductivity in W/K m at 1 K [3.127]. More exactly

$$\kappa = (RRR/0.76)T[W/K\mathrm{m}] \quad \text{and} \quad \kappa = (RRR/0.55)T[W/K\mathrm{m}] \qquad (3.46)$$

for Cu and Ag, respectively (but see the above discussion and Fig. 3.24). Typical values for the thermal conductivity of Cu and Al at different purities are 10^2 to 10^3 (10^2 to 10^4; 10^3 to 4×10^4) W/K m for 4 N (5 N; 6 N) purity, annealed (400°C) Al, and 50 to 200 (200–5,000) for 4 N (5 N) annealed Cu [3.127, 3.128]. Information on the thermal conductivity of a large number of Al alloys for temperatures between 2 K and room temperature can be found in [3.129]. At 1 K, they are typically between 1 and 3 $\mathrm{W\,K^{-1}\,m^{-1}}$.

Because of the importance of copper and of other noble and platinum metals for making high-conductivity thermal joints (or for thermometry purposes; see Sects. 12.9, 12.10), I shall discuss a process by which magnetic impurities can be "passivated" in Cu, Ag, Au, Pt, Pd, Rh and possibly some other metals as well, by oxidizing the less noble metal impurities, resulting in a dramatic increase of the low-temperature conductivities. The following discussion applies to the "passivation" of the magnetic scattering of iron in copper [3.130–3.133] (for Ag, see [3.134]).

The typical residual resistivity ratio of a piece of copper which one can buy from a shop is in the range of 50–100. Heating the copper to a temperature of 400–500°C anneals structural lattice defects, and the residual resistivity ratio usually increases to a value of 300–400. A further increase is only possible by passivation of magnetic impurities, in particular by oxidation of iron. The less noble impurities are oxidized by heat treatment of the Cu specimen at a temperature of 900–1,000°C in an atmosphere of oxygen or air at 10^{-5}–10^{-4} mbar (the time required for this treatment depends mainly on the thickness of the Cu sample). This oxidation and passivation is a two-step process. In the first step Fe is oxidized to FeO by oxygen diffusing through the Cu matrix.

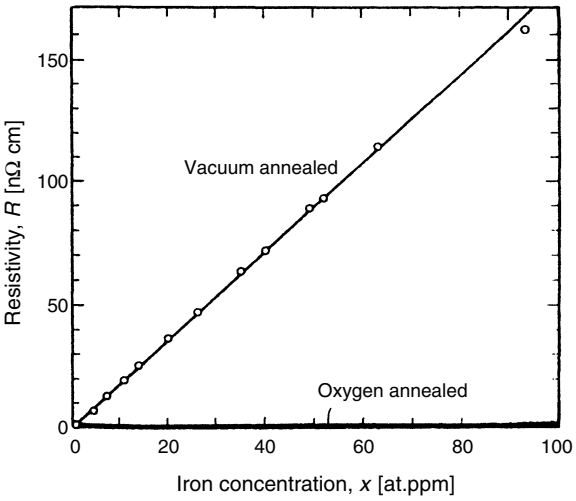

Fig. 3.26. Resistivity of Cu–Fe at 4 K, as a function of Fe impurity concentration, annealed in vacuum and in an O_2 atmosphere (92 h; about 10^{-6} bar air) [3.130]

FeO is stable, whereas copper oxide is unstable at these temperatures. The iron oxides attract more FeO and O and create small (0.1 μm) Fe_3O_4 clusters, reducing the number of magnetic scattering centres. These clusters are magnetically ordered; the conduction electrons do not suffer spin-flip scattering at the fixed iron moments any more. In this sense, the iron moments are magnetically inactive for the scattering of conduction electrons of the host lattice. Thus, although the Cu is not purer after oxygen annealing, the impurities are much less effective as scattering centres (Fig. 3.26).

Another very effective purification of Cu from Fe reported in the literature is an electrolytic process starting from a Cu sulphate solution, followed by a wet-hydrogen treatment to remove nonmagnetic impurities [3.135]. The residual hydrogen has then to be "pumped out" by heating the Cu in vacuum at around 1,000°C. The resulting increased conductivity corresponds to a residual resistivity ratio of at least 1,000 and in extreme cases up to several 10,000, at which point dislocation scattering of the conduction electrons dominates.

Of course, it is an advantage if the starting copper already contains oxygen; oxygen-free high-conductivity (OFHC) Cu is often not well-suited for the production of high-conductivity copper needed for low-temperature experiments. However, it has been shown that oxygen annealing can be detrimental for the conductivity of commercially available ultrapure (7N) Cu [3.136].

Oxygen annealing does not change the conductivity of Al because of the very small magnetic moments of 3d-elements in Al.

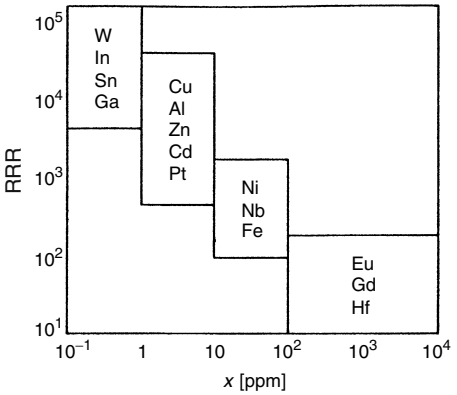

Fig. 3.27. Typical values of the residual resistivity ratio (RRR) of various metals as a function of typical impurity concentrations with which they are available [3.138]

A survey on the transport properties of pure metals in the defect scattering limited range and a compilation of the smallest residual resistivities which have been reported in the literature for all metals except the rare earths can be found in [3.137]. Figure 3.27 gives typical values of the residual resistivity ratio which one can attain in pure metals as a function of the impurity concentration. Comprehensive compilations of data on the thermal conductivity of solids can be found in [3.44, 3.45, 3.90–3.93]. Values for metallic elements at 273 K are compiled in [3.87], p. 28.

3.3.8 How to Measure Thermal Conductivities

Usually, the thermal conductivity of a material is determined by measuring with two thermometers the temperature difference produced by heating one end of it and keeping the other one at the constant temperature of a heat sink (see [3.86, 3.87] and references therein). This simple steady-state method has several pitfalls and problems that are rather similar to the ones in measurements of heat capacities (see Sect. 3.1.8). For example, heat losses by radiation and into eventually still remaining gas molecules in the surrounding, Joule heating in the thermometers, parasitic heat leaks along leads to heater and thermometers, the thermal resistances of them to the sample; etc (see also Sect. 5.1.2). The heat flow along the leads can be strongly reduced by using thin superconducting wires at their low-temperature end and by properly heat sinking them. Radiation losses are particularly problematic at higher temperatures. They can be substantially reduced by using radiation shields around the setup at a temperature close to the samples temperature [3.33, 3.58], or by applying the so-called 3ω-method introduced by [3.139]. This method uses a radial AC heat flow into the sample from a heated narrow

metal film deposited onto it. This metal strip serves as heater as well as thermometer. A current of frequency ω through it heats the sample with a power at a frequency 2ω. The resulting resistance or temperature oscillations of the metal strip at 2ω times the driving current at ω results in 3ω-oscillations in voltage across the metal strip that are measured as the third harmonic of the voltage by a lock-in amplifier. A challenge in applying this technique is the measurement of the small 3ω-signal in presence of the much larger background signal at ω. To determine the thermal conductivity of the sample, measurements at several frequencies have to be performed. Besides essentially avoiding radiation losses, the measurement needs only a few periods of temperature oscillations. Hence, data are obtained rather fast and can be taken while warming or cooling the sample. The 3ω-method is also quite suited for measuring the thermal conductivity of thin films, however, it then requires special design and data analysis considerations [3.87, Chap. 2.2].

For choice of appropriate thermometers and heaters the considerations are again rather similar as discussed in the above section for heat-capacity measurements. For the heater, of course, a material with temperature-independent resistance, like phosphor bronce, TiCr, or NiCr alloys, should be chosen.

The problems of parasitic heat dissipation and thermal shunts or losses through the electrical leads to heater and thermometers have been substantially reduced in two recent experiments in which the thermal conductivity of badly conducting glasses have been measured down to 5 mK. In the first one [3.96], the dielectric constant of the glass sample itself was used for thermometry (see Sect. 12.8) and the parasitic power dissipation was reduced to about 0.1 pW. This method avoids any thermal boundary resistance between thermometers and sample. The careful anchoring of the leads (resulting in less than 0.1% of heat loss) and calibration of the dielectric constant thermometers are discussed. In the second experiment [3.97], thermometry was performed by measuring in a second-order axial gradiometer (to avoid magnetic contributions from the sample) inductively the change of DC magnetization of two paramagnetic $Au\mathrm{Er}_{500\mathrm{ppm}}$ strips glued to the sample. The gradiometer leads are directly connected to the input of a SQUID, resulting in extremely low power dissipation (see Sect. 12.9). Because heat is applied optically from a light emitting diode to one end of the sample, the method is contact-free, reducing the parasitic heat leak to below 10^{-15} W (Fig. 3.28). Data obtained by these methods are mentioned in the caption of Fig. 3.22. One may have to resort to these or other more elaborate techniques [3.86, 3.87], particularly if thermal conductivities of small samples or of thin films have to be measured. For these cases, microfabricated heaters and thermometers or optical excitation and possibly also detection methods may have to be used. As for a heat-capacity apparatus, the quality of a thermal conductivity setup can be checked by investigating a well-characterized standard sample. Another appropriate check of the validity of the obtained data is a measurement of the thermal conductivity at various heat flows.

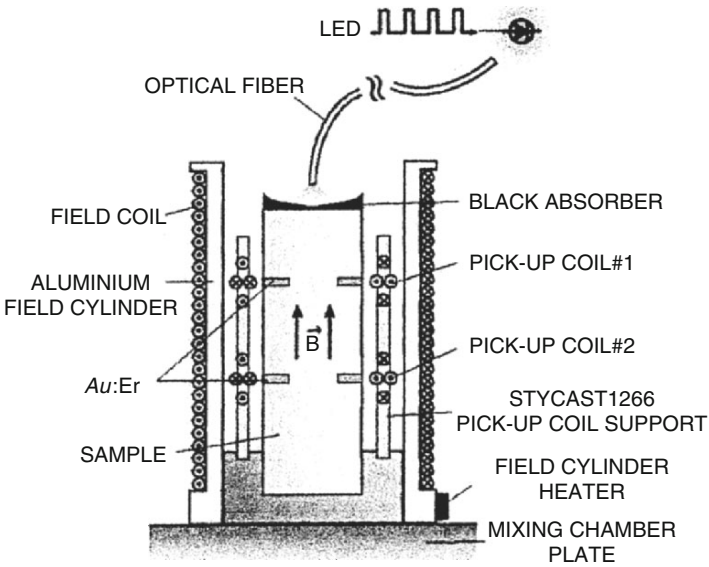

Fig. 3.28. Schematic of a setup to measure contact-free thermal conductivities at millikelvin temperatures. The temperature gradient in the sample is generated by cooling one end with a dilution refrigerator and heating the other one optically with a light emitting diode kept at 1 K. The temperatures are determined by measuring inductively in second order gradiometers the susceptibility of two paramagnetic $Au\mathrm{Er}^{+}$ pieces (see Sect. 12.9) glued to the sample. The superconducting Al shield can be heated above its critical temperature for a short time to freeze in the measuring field of 0.5 mT. Reprinted with permission from [3.97]; copyright (2004), Am. Inst. Phys.

3.4 Magnetic Susceptibilities

3.4.1 Magnetic Susceptibilities of Some Selected Materials

This section gives representative data for the magnetic susceptibility of various materials, in particular of weakly magnetic materials often used in the construction of cryogenic apparatus where sensitive magnetic measurements are to be performed. In Table 3.5 the parameters x_∞ and C of the equation

$$\chi/\rho = x_\infty + C/T \tag{3.47}$$

for the susceptibility χ per mass density ρ are given. The given data have been obtained in different temperature ranges. One should keep in mind that a variation of χ can be found in the literature for some of the listed materials, particularly weakly magnetic, multicomponent materials. This can be partly explained by slight differences in the composition and/or in the preparation of nominal identical materials. For details, see the original publications [3.140–3.146].

Table 3.5. Susceptibility of some selected materials

material	C $[10^{-6}\,\mathrm{emu\,K/g}]$	x_∞ $[10^{-6}\,\mathrm{emu/g}]$	Refs.
Fused quartz, Suprasil	0.05 ± 0.02	-0.383 ± 0.004	[3.140]
Macor	24.5 ± 0.06	2.87 ± 0.18	[3.140]
Stycast 2850 GT	17 ± 1	2.97 ± 0.15	[3.140]
	26 ± 7	15 ± 4	[3.141]
Stycast 1266	0.63 ± 0.03	-0.18 ± 0.01	[3.140]
Epibond 1210 A/9615-10[1]	80 ± 4	7.0 ± 0.4	[3.140]
GE varnish 7031, cured	2.2 ± 01	-0.54 ± 0.03	[3.140]
Mixed 1:1 with toluene	-7 ± 3	2 ± 1.5	[3.141]
Apiezon N grease	-2 ± 3	0.1 ± 1.2	[3.141]
Mylar tape	0.34 ± 0.02	-0.43 ± 0.02	[3.140]
Teflon tape	0.063 ± 0.003	-0.33 ± 0.02	[3.140]
	0.05 ± 0.01	-0.33 ± 0.01	[3.142]
Nylon	-0.06 ± 0.02	-0.63 ± 0.01	[3.142]
	0.3 ± 3.0	-0.6 ± 1.5	[3.141]
Manganin wire (low Ni)	(318)	92 ± 5	[3.140]
Manganin wire, enamel insulated	-13 ± 3	120 ± 1	[3.141]
$Cu_{0.7}Ni_{0.3}$ (Inconel)	$(-2.3 \pm 0.2) \times 10^5$	$(2.6 \pm 0.2) \times 10^5$	[3.141]
Stainless steels	-120 to ± 10	100 to 300	[3.141]
$Pt_{92}W_8$, alloy 479	0.43 ± 0.02	0.24 ± 0.01	[3.140]
AR glass	36 ± 1	-0.35 ± 0.01	[3.143]
Duran glass	15.8 ± 0.5	-0.40 ± 0.01	[3.143]
Suprasil glass	0.01 ± 0.01	-0.40 ± 0.01	[3.143]
Gelatine	1.0 ± 0.1	-0.41 ± 0.01	[3.143]
AR glass	29 ± 3		[3.143]
Duran glass	5.7 ± 0.6		[3.143]
Suprasil glass	< 0.01		[3.143]

Data are taken at: 2–10 K [3.140]; 4.2 K [3.141, 3.142]; > 5 K for first set, < 0.1 K for second set of data of [3.143]

In addition to the data given in Table 3.5, remanent magnetic moments and susceptibilities for a large number of metals, dielectrics, wires and ribbons as well as for some further materials used in the construction of cryogenic equipment can be found in [3.144] for $T = 2$ K, and in [3.145] for $T = 4.2$ K. The most recent publication on this topic is [3.146], where the results obtained for the magnetization of 13 materials at 2–12 K and at 0.25–4 T have been presented. Some of these data are shown in Fig. 3.29. Data for various austenitic stainless steels (AISI 300 series 304, 310, 316, and AWS 330) at 4.2–414 K are given in [3.147]. Typical parameters for (3.47) are $\chi_\infty = 16(11;0)$ and $C = 3(4;11)$ for AISI 304/316(310S;AWS 330).

It is remarkable that a large number of materials which are usually considered as "nonmagnetic" show quite appreciable values for their susceptibilities and remanent magnetizations at low temperatures, often making them

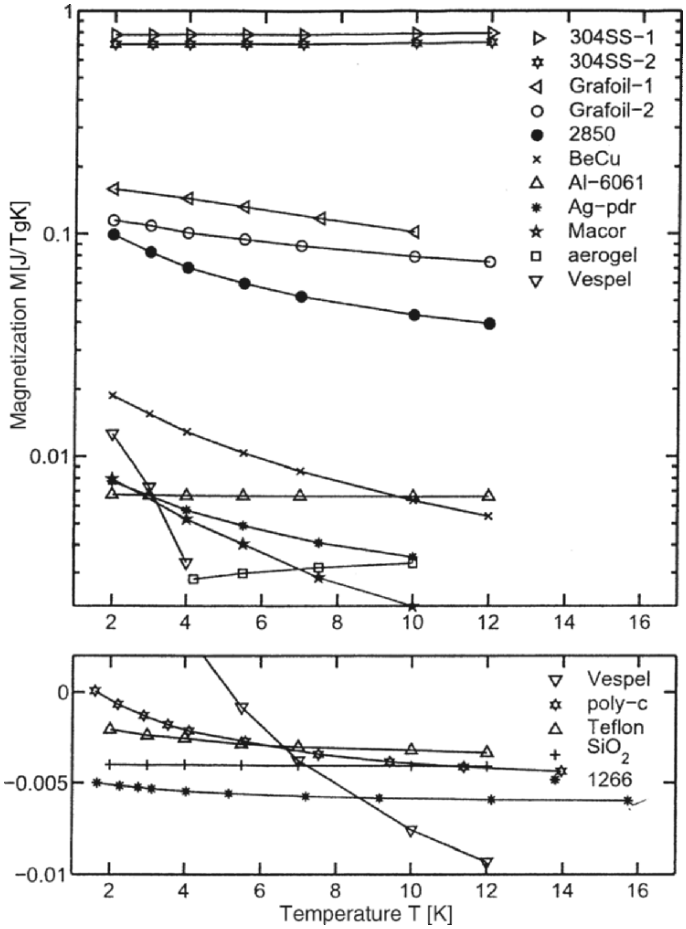

Fig. 3.29. Magnetization per mass (J/TgK) of the indicated materials in a field of 1 Tesla. The upper graph is logarithmic and shows data for paramagnetic samples. The lower graph is linear and shows data for diamagnetic materials [3.146]

unsuitable for use in magnetically sensitive equipment or experiments. From the shown data, one can conclude that the fused glass Suprasil is essentially free of magnetic impurities (substantially less than 1 ppm; quite different from other glasses!) and has a very low susceptibility [3.43, 3.104] (Fig. 3.30), making it a very good candidate for many applications, for example as sample holder in susceptometers or for experiments in high magnetic fields. Other candidates with somewhat higher but still low concentration of magnetic impurities seem to be cotton thread and dental floss, as well as Teflon and Nylon (see Table 3.5).

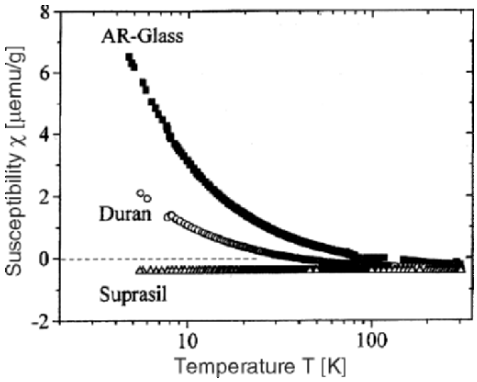

Fig. 3.30. Susceptibility of three different glasses as a function of temperature in a field of 1 T, demonstrating the purity of Suprasil glass. Reprinted from [3.143], copyright (1995), with permission from Elsevier

3.4.2 How to Measure Susceptibilities and Magnetizations

The Conventional Method

Surely, the simplest and most common method to measure the magnetic susceptibility of a material is to wind a sensitive pick-up coil (for example, some 1,000 turns of 25 μm Cu wire) around it, apply a magnetic field at a frequency between 0.1 and 1 kHz (by a superconducting coil of 0.1 mm NbTi wire, for example) to it and measure the signal induced in the pick-up coil by a home-made (for example, using a lock-in amplifier or for more sensitive measurements a SQUID, see below) or by a commercial inductance bridge. This is also the method applied to detect superconducting transitions, for example in superconducting fixed-point-devices (see Sects. 11.4.2 and 11.4.3), or for measurements of susceptibilities of samples down to milli- or even microkelvin temperatures. A setup in which several samples can be investigated in one run is shown in Fig. 3.31. It has been used for measurements to 25 μK [3.122]. Examples of electronic setups for measuring susceptibilities using either a lock-in amplifier in a self-inductance bridge or a SQUID as detector for more sensitive measurements are shown in Figs. 3.32 and 3.33. To avoid heating effects due to relaxation in the sample or from eddy currents, a bridge should be operated at low enough frequency, for example in the range of 20–300 Hz. This will also reduce capacitance leakage effects. Another suitable setup for determination of susceptibilities measures the resonant frequency in the range of 1 MHz of a tank circuit driven by a tunnel diode whose inductance contains the paramagnetic sample [3.148, 3.149]. More sophisticated methods, in particular the application of a SQUID as detector as well as commercial versions of magnetometers will be discussed in more detail below.

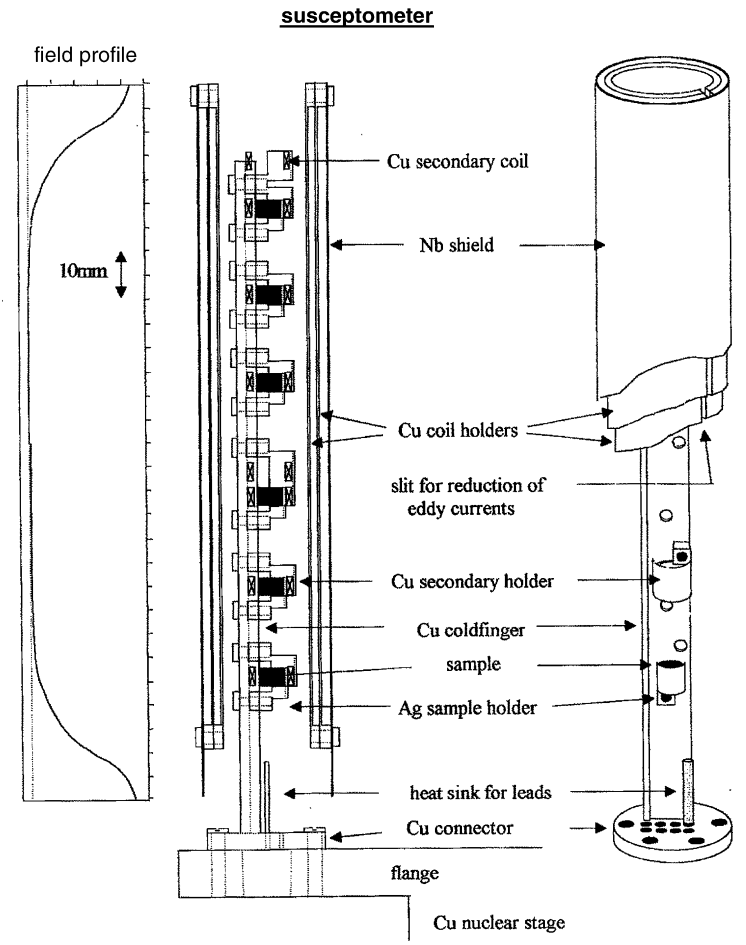

Fig. 3.31. Schematics of a susceptometer cooled by a Cu nuclear refrigeration stage (Sect. 10.8). It is designed for simultaneous investigation of six samples down to microkelvin temperatures. The two empty coils are used as a reference. In addition, the profile of the applied static field is shown; the field coil is surrounded by a superconducting Nb shield (Sect. 13.5.2), [3.122]

If an inductance measurement is performed, then the following relations are relevant. In the primary coil we generate a current $I = I_0 \sin(\omega t)$ which produces a change of magnetic flux

$$\frac{\mathrm{d}\phi_1}{\mathrm{d}t} = \frac{A_1(\mathrm{d}I/\mathrm{d}t)N_1^2}{L_1}\,, \tag{3.48}$$

where A_1 is the area, N_1 the number of windings and L_1 the length of the primary coil. This flux change induces a voltage in the secondary coil given by

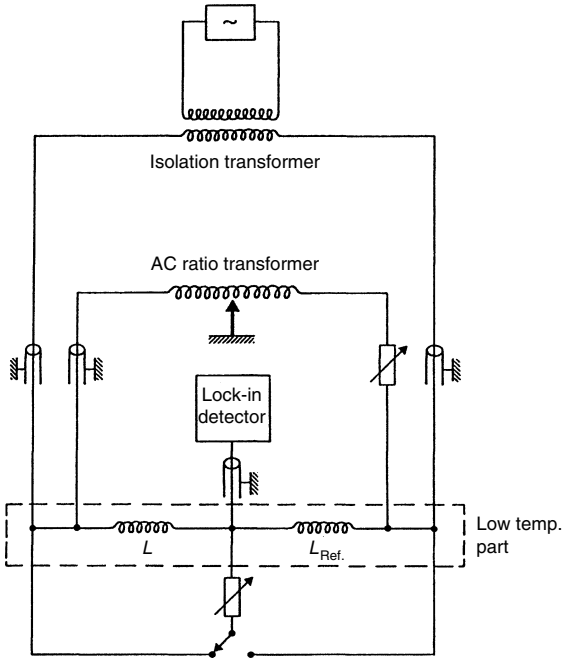

Fig. 3.32. Self-inductance bridge to measure magnetic susceptibilities

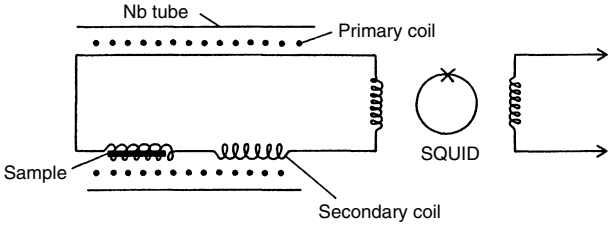

Fig. 3.33. Circuit to measure magnetic susceptibilities with a SQUID. The design uses an astatic pair of pick-up coils with the sample in one of them. Because of the high sensitivity of the SQUID a few milligrams of a paramagnetic material is sufficient. The astatic pair, which can be made with an accuracy of about 1%, reduces the sensitivity of the device to external disturbances and also compensates the influence of the magnetization of the construction materials. The principle of the design is to keep the total flux constant, which makes it necessary to make the low-temperature wiring from a superconducting material [3.45, 3.151]

$$U_2 = \mu_0(1+\chi)\frac{N_1 N_2 A_2 \omega I_0}{L_1}\cos(\omega t)\,, \tag{3.49}$$

where A_2 is the area, N_2 the number of windings of the secondary coil, and χ is the temperature dependent susceptibility of the sample in the secondary coil.

The mutual inductance of two secondary coils sitting inside of a primary coil and with one of them containing a cylindrical sample of susceptility χ is [3.150]

$$M_{\mathrm{s}} = \pi\mu_0 n_{\mathrm{p}} n_{\mathrm{s}} r_{\mathrm{s}}^2 f_1 (1 - D + f_2) q\chi \tag{3.50}$$

with $n_{\mathrm{p(s)}}$ being the number of turns per cm of the primary (of one of the secondary) coil, r_{s} the radius of the sample, D the mean demagnetization factor (typically 1/3), and q the filling factor of the sample in one of the secondary coils (typically 1/2). The geometric factors f_{i} depend on the lengths of the sample, primary and secondary coils, and were given in [3.150]. A similar equation for a spherical sample in one of the secondary coils can be found in [3.151]. In all these measurements care must be taken to determine the isothermal ($\omega\tau \ll 1$) and not the adiabatic susceptibility.

All the described methods, of course, "see" not only the sample but all other magnetization in the neighbourhood as well hence one should avoid other magnetic materials rather carefully or choose a design so that their contributions are cancelled, for example, as is the case in a carefully wound astatic pair of secondary coils. For very high-sensitivity measurements one may even consider to regulate the temperature of these coils.

For all the discussed methods one should carefully choose a "non-magnetic" sample holder, like Suprasil glass (see Sect. 3.4.1), in a symmetric setup to reduce background contributions to the signal. In addition, in the analysis of the data, one may have to consider demagnetization effects and the contribution from the Weiss field (see Sect. 12.9).

Vibrating – Sample Magnetometers

An alternative method is the use of a vibrating-sample magnetometer. Here, a sample oscillates inside of a coil and the induced voltage is proportional to the magnetic moment of the moving sample. According to my knowledge, the most recent design of an automated vector vibrating-sample magnetometer can be found in [3.152]. It allows rotating the sample against the applied magnetic field so that the angular dependence of longitudinal, the transversal and the total magnetization can be measured. Using lock-in techniques, the sensitivity is $5{\times}10^{-6}$ emu at 4.2–340 K in fields up to 2 T and at vibration frequencies of 42 Hz. The authors stress the vibration isolation and the detection system consisting of six coils.

Vibrating sample magnetometers are available commercially.

SQUID Magnetometers

With the advancement and the commercial availability of the SQUID, very sensitive SQUID magnetometers have become a quite common instrument to

measure susceptibilities and magnetizations. In this device, a superconducting coil (made from 0.1 mm NbTi wire, for example) is wound around the sample to measure its magnetic moment. This coil and the input coil of the SQUID are parts of a closed superconducting loop acting as a flux transformer. The setup is surrounded by a superconducting magnet to provide a small magnetic field for the measurement. Any change in the permeability of the circuit from a change of the magnetic properties of the sample will result in a screening current to keep the total flux constant and will therefore produce a flux change in the input coil to the SQUID. This change can be produced by moving the sample in the pick-up coil – the conventional operation of commercial SQUID magnetometers – or by changing its magnetization due to a temperature change. In general, the pick-up coil is wound as a second-order gradiometer with the two outer loops wound oppositely to the two central loops to reduce spurious influences. Changes as small as 10^{-4} flux quanta can be measured. The part of the superconducting loop connecting the pick-up coil and the input coil of the SQUID should be tightly twisted and shielded by a superconducting capillary of Nb, for example, to reduce flux changes from external disturbances. A further useful precaution is a low-pass filter on the pick-up coil. Usually, the SQUID is used as a nullmeter to increase sensitivity and the dynamic range to several orders of magnitude as well as to avoid currents circulating in the coils. This is achieved by adding a feedback coil, which produces a compensating flux or voltage. This compensating voltage is measured as a function of position or temperature of the sample. A heater at one point of the superconducting loop can raise its temperature above T_c to eliminate unwanted trapped flux when preparing the setup for the next measurement.

A very good recent design of a home-built, fully automated SQUID magnetometer for operation in combination with a ^{3}He-^{4}He dilution refrigerator has been described in [3.153]. The refrigerator contains a specially designed plastic mixing chamber that allows the sample to be thermalized directly by the ^{3}He flow to 10 mK. The measuring equipment is based on a DC-SQUID coupled to a second-order gradiometer coil system. To measure a magnetic moment, the sample is moved through the gradiometer coils by smoothly lifting the whole dilution refrigerator. The noise of the setup in operation translates to a magnetic noise of 10^{-6} emu. The paper includes details on grounding and shielding as well as on minimizing eddy current effects. The relevant equations for converting the flux indicated by the SQUID and its electronics to the magnetic moment of the sample can be found there as well as in [3.45], for example.

Of course, if no special features, like ultra-low temperatures or very high magnetic fields, of the magnetometer are required and if the necessary funds are available, one should buy one of the commercially offered fully automatic, very flexible and powerful SQUID magnetometers or magnetic-property-measurement systems. They are offered for the temperature range of 1.8–400 K (optionally to 0.5 [3.154] and to 800 K) and for fields up to 7 T. These systems

allow setting of temperature and field sequences as well as of particular operation modes, for example, for the motion of the sample and/or for the SQUID, and allow fully automated around-the-clock operation. In these systems, the SQUID output, i.e., the pick-up coil signal as a function of the samples position, is fitted to the expected theoretical response of a magnetic dipole. Eventually, this ideal response curve is compared to the systems calibration, and the sign and value of the samples magnetic moment are calculated. The volume or mass susceptibility can then be calculated from this moment. The resolution for magnetic moments reaches $1\times(5\times)10^{-8}$ emu at zero (7 T) field for moments up to 5 emu; optionally, moments up to 300 emu can be measured.

A quite common problem of these instruments has been discussed and investigated in [3.155,3.156]. It arises from the assumption in the analysis that the magnetic moment of the sample does not change during the measurement. However, in its movement through a non-homogeneous field, a superconducting sample, for example, will follow a hysteresis loop, resulting in a position-dependent magnetic moment of it. The moment calculated by the software of the magnetometer will then not represent the actual moment of the sample. An example of such a situation is shown in Fig. 3.34. The shown features arise from field inhomogeneities of the order of 0.1 mT only. This is well within the change of remanent fields of superconducting magnets over the scan length of the magnetometer, and is usually within the range of the field homogeneity

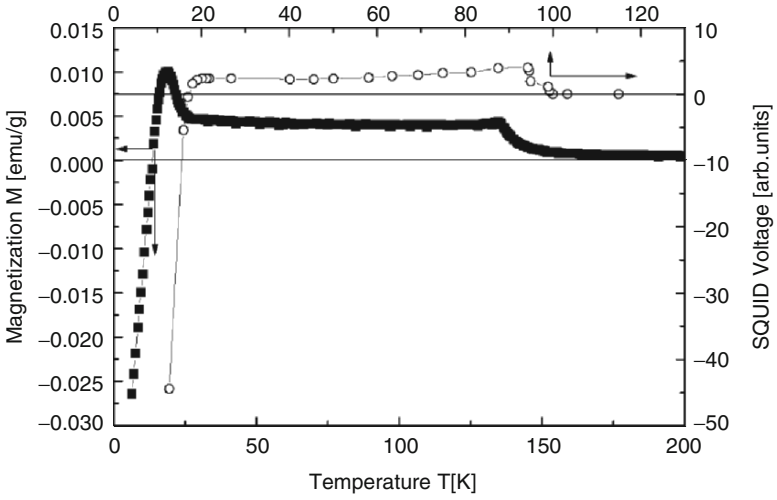

Fig. 3.34. Zero-field cooled DC magnetization measured in a commercial SQUID magnetometer by moving the sample $RuSr_2GdCu_2O_3$ in a field of 0.25 mT through the pick-up coil system of the magnetometer. The magnetization shows an apparent peak at temperatures below $T_c = 30$ K (■). When measuring the output voltage of the SQUID circuit as a function of temperature without moving the sample in the magnetometer no peak like feature is observed (◯) [3.155]

claimed by the supplier of the instrument. Of course, the remanent field can change from one cycle to the next one of the magnet. The obtained apparent moment of the sample will then depend on the field profile and its sign as well as on the scan length in the magnetometer and the properties of the sample. A first check whether the mentioned problem occurs is an inspection of the symmetry of the output signal of the SQUID. However, sometimes the deformations of the signal can be rather small but still creating significant errors in the data. The most reliable test is to measure the magnetic moment of the sample without moving it, for example just as a function of temperature, if the magnetometer offers such an option.

Of course, SQUID magnetometers are in general not practical in experiments at very high magnetic fields. This is an area where the magnetometers to be discussed below have become of particular importance.

Micro-Torsional and Cantilever Magnetometers

In Sect. 13.10 I will discuss very sensitive torsional and translational devices that have been developed to mechanically measure a variety of properties of liquid and solid samples. Most of these devices can be used to measure the magnetic properties of a sample as well by just mounting (or evaporating) the sample onto the moving part and measuring the induced voltage inductively by a pick-up coil or capacitively by an electrode (see Fig. 13.19). The measurement relies on the fact that a sample with a magnetic moment m in an external magnetic field B experiences a torque

$$\tau_m = mB. \tag{3.51}$$

Hence, the torque τ in the equations of Sect. 13.10 has to be replaced by $\tau + \tau_m$. For the measurement, an AC magnetic field at the resonance frequency of the oscillator in the low-kHz range is applied at an angle to the magnetization of the sample to drive the oscillator. In most cases micro- or even nano-mechanical devices are used. The advantage of their small size – besides their sensitivity and simplicity – makes them particularly useful in difficult environments, such as very low temperatures or very high magnetic fields.

For example, in [3.157] a two-stage, high-Q silicon torque magnetometer was described that is just a torsional oscillator as discussed in Sect. 13.10.4 (see Fig. 13.19) but with a magnetic sample mounted or evaporated onto the oscillating head. The small torsional spring constant of the oscillator (typically 10^{-2} N m) combined with its high Q-value of typically 10^6 allow detection of magnetic moments as small as 10^{-10} emu (10^{-13} J T^{-1}). These magnetometers can either be used by measuring the deflection, where a sensitivity for displacement of less than 0.1 nm has been achieved [3.157], or by measuring, with an accuracy of 10^{-8}, the shift in resonant frequency due to the

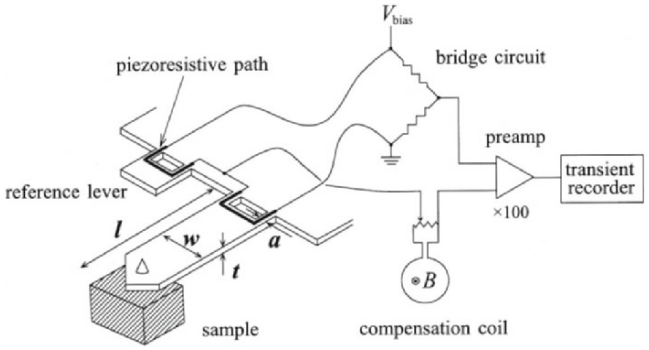

Fig. 3.35. Schematics of a torque magnetometer consisting of a commercial piezoresistive cantilever – to which a sample is connected – with a reference cantilever, a detecting bridge circuit, and a compensation coil. Reprinted with permission from [3.159], see this reference for details; copyright (2002), Am. Inst. Phys.

anisotropy of magnetization of a sample [3.158]. The latter magnetometer was designed for use in magnetic fields up to 25 T with an accuracy of 2×10^{-8} emu ($2\times10^{-11}\,\mathrm{J\,T^{-1}}$).

In [3.159], a miniature high-frequency torque magnetometer has been described, which has been successfully used to investigate the magnetic properties of sub-μg samples in pulsed (!) magnetic fields up to 38 T with pulse durations of 30 or 60 ms. This magnetometer (Fig. 3.35) consists of a small cantilever with the sample mounted on its free end. Sensitivities – limited by the mechanical noise from the pulsed magnet – of about $10^{-11}\,\mathrm{N\,m}$ for the torque and 5×10^{-10} emu for the magnetic moment have been reached; 10^{-11} emu should be possible in a field of 10 T produced by a much more quiet superconducting magnet, which is higher than for a SQUID magnetometer. The authors used commercially available piezoresistive silicon microcantilevers (produced for atomic force microscopy) with eigenfrequencies of 250–300 kHz and spring constants of 30–40 $\mathrm{N\,m^{-1}}$. These rather high frequencies strongly reduce the disturbances from externally induced vibrations, for example from pulsing the strong magnetic field; a longer cantilever with about seven times lower eigenfrequency did behave considerably worse, for example. The mass of the sample should be small enough to keep the eigenfrequency of the setup higher than the frequency of the signal. A reference cantilever is used to cancel background signals from the temperature and field dependencies of the cantilever (Fig. 3.35). A compensation coil is used to eliminate $\mathrm{d}B/\mathrm{d}t$ signals caused by the rapid field sweep. A result of a measurement using this magnetometer is shown in Fig. 3.36. Of course, the cantilever can also be used as a microbalance to determine the mass of the usually quite small samples by just measuring the shift of the eigenfrequency when the sample is mounted on it (see Sect. 13.10.4).

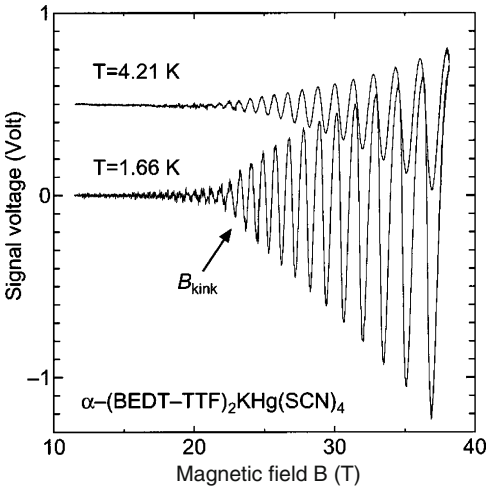

Fig. 3.36. Signal voltage proportional to the magnetic torque of 10 μg of the indicated quasi-two-dimensional organic conductor at two temperatures as a function of magnetic field. The measurements have been performed with the piezoelectric torque magnetometer shown in Fig. 3.35. The oscillations in magnetization – periodic in inverse magnetic field – are due to the de Haas–van Alphen effect resulting from the discrete Landau levels of the electronic energy in an external magnetic field. At low temperatures the compound undergoes a transition ("kink transition") from a charge density-wave to a metallic state at 23 T. Reprinted with permission from [3.159]; copyright (2002), Am. Inst. Phys.

In [3.157–3.159] one can find references to former work using microcantilever magnetometers – usually for much lower frequencies than just discussed – and in particular for applications in steady magnetic fields.

Problems

3.1. Verify that (3.9) is the valid result in the approximation $T < \Theta_D/10$.

3.2. Calculate the Debye temperature of solid Argon (see Fig. 3.2b).

3.3. The atomic weight of Cu is 63.55 and its density is 8.93 g cm^{-3}. Calculate its Fermi temperature.

3.4. Calculate the Fermi temperature of liquid ^{3}He.

3.5. Under which condition does the Fermi–Dirac distribution function (3.11) change to the Maxwell–Boltzmann distribution function?

3.6. At which temperature do the lattice and conduction–electron contributions to the specific heat of copper become equal?

3.7. At which temperature is the magnetic contribution (3.20) in a field of 100 mT equal to the conduction–electron contribution to the specific heat of Ag [for material parameters of Ag, see Table 10.1; use (10.3, 10.4)]?

3.8. Calculate the temperature at which the specific heat of aluminum in its superconducting and its normal state become equal, see Fig. 3.5 a,c, and Table 10.1.

3.9. Calculate the wall thickness of a $Cu_{0.7}Ni_{0.3}$ tube of 6 mm diameter, which has the same thermal conductivity as a 10 mm diameter Teflon rod at 1 K (Table 3.2).

3.10. What should be the inner diameter of a $Cu_{0.7}Ni_{0.3}$ capillary of 1 mm wall thickness filled with solid ^{4}He at 0.3 K so that its thermal conductivity is equal to that of the solid ^{4}He in it (Fig. 3.21)?

3.11. Calculate the temperature at the "hot" end of a cylindrical rod of 20 mm length and 2 mm diameter, if it is heated with 0.1 nW and the cold end is kept at 0 K. Carry out the calculation for a plastic, for brass and for Cu (see Fig. 3.21 for thermal conductivities).

3.12. At which temperature are the thermal conductivities of Cu($\propto T$) and of liquid ^{3}He at SVP ($\propto T^{-1}$) become equal, see Figs. 2.18 and 3.21?